

An ab initio study of the band gap of high-entropy silicides based on FeSi_2

Jørn-Marcus Høylo-Rosenberg



Thesis submitted for the degree of
Master in Materials Science for Energy and
Nanotechnology
60 credits

Department of Chemistry
Faculty of mathematics and natural sciences

UNIVERSITY OF OSLO

Spring 2022

An ab initio study of the band gap of high-entropy silicides based on FeSi₂

Jørn-Marcus Høylo-Rosenberg

© 2022 Jørn-Marcus Høylo-Rosenberg

An ab initio study of the band gap of high-entropy silicides based on FeSi₂

<http://www.duo.uio.no/>

Printed: Reprosentralen, University of Oslo

Abstract

Contents

1	Introduction	1
I Theory		3
2	High-Entropy alloys	4
2.1	Fundamentals	4
2.2	Core effects and properties	7
3	Modeling of random alloys	9
3.1	The Special Quasi-random Structure model	9
3.1.1	Mathematical description	10
3.1.2	Applications to high-entropy alloys	12
4	Density Functional Theory	16
4.1	Review of Quantum Mechanics	17
4.1.1	The Shrödinger equation	17
4.1.2	Approximations to the many-body Shrödinger equation	18
4.2	Kohn-Sham density functional theory	20
4.2.1	Density functional theory	20
4.2.2	The Kohn-Sham Equation	21
4.3	Limitations of DFT	22
II Method		24
5	Practical aspects of DFT	25
5.1	The Exchange-Correlation functional	25
5.1.1	Local density approximation	26
5.1.2	Generalized gradient approximation	26
5.1.3	Meta-GGA	26
5.1.4	Hybrid functionals	27
5.1.5	Outlook	28
5.2	Plane waves and reciprocal space	28
5.3	Self-consistent field calculation	31

6 Computational details	32
6.1 Settings and dependencies	32
6.2 Material	33
III Results and Discussion	35
7 The high-entropy silicide (CrFeMnNi)Si₂	36
7.1 β -FeSi ₂	36
7.2 (CrFeMnNi)Si ₂	37
7.2.1 The band gap	39
7.2.2 Local and projected density of states	42
7.2.3 The band gap with SCAN and HSE06	45
7.2.4 Pair distribution functions	50
7.2.5 Charge density	51
7.2.6 SQS size	52
8 Alternative compositions	56
8.1 Exploring the quaternary phase diagram	56
8.2 High entropy silicides with cobalt/titanium	60
8.3 Negative systems	64
IV Conclusion and future work	66
9 Conclusion	67
10 Future work	69
A Figures	70
A.1 Density of states	70
A.2 Projected density of states	72
A.3 Charge density	73

List of Figures

2.1	Formation of HEA based on δ and N . Figures adopted from [heav2016_ch2]	6
2.2	A schematic illustration of lattice distortion in high-entropy alloys. Figure from [owen_jones_2018]	8
3.1	PDFs of (a) 20 and (b) 250 atom SQS models of CrFeMnNi [heav2016_ch10]	13
3.2	Density of states with SQS and MC/MD of FCC CoCrFeNi, figure from [heav2016_ch10]	14
3.3	Probability distribution functions with SQS and MC/MD of HCP CoOsReRu [heav2016_ch10]	14
4.1	Number of DFT studies per year from 1980 to 2021 [dimensions].	16
5.1	Jacob's ladder [jacob].	25
5.2	Calculated to experimental band gap measurements of Becke-Johnsoon, modified Becke-Johnson and SCAN functionals [xc_benchmark]	27
5.3	Self consistent iterations of a DFT calculation. Figure adopted from the lecture notes in FYS-MENA4111 [persson2020] .	31
6.1	Five distinct 48-atom SQSs of $\text{Cr}_4\text{Fe}_4\text{Mn}_4\text{Ni}_4\text{Si}_{32}$ based on the $\beta - \text{FeSi}_2$ crystal structure. Manganese atoms are represented as purple spheres, chromium as dark blue and silicon as light blue, followed by iron and nickel presented as gold and silver spheres respectively. The respective SQSs are denoted as A, B, C, D and E. Figures illustrated with VESTA [vesta] .	34
7.1	Density of states [states/eV] of $\beta\text{-FeSi}_2$	37
7.2	Density of states [states/eV] of SQS D of $(\text{CrFeMnNi})\text{Si}_2$	39
7.3	Density of states [states/eV] of SQS B of $(\text{CrFeMnNi})\text{Si}_2$	39
7.4	Density of states [states/eV] of SQS A of $(\text{CrFeMnNi})\text{Si}_2$	40
7.5	Local density of states [states/eV] of Si (SQS D)	43
7.6	Local density of states [states/eV] of (a) Cr, (b) Mn, (c) Fe, (d) Ni in SQS D.	43
7.7	Projected density of states [states/eV] of SQS D.	44
7.8	Projected density of states [states/eV] of SQS D and B around E_F	44

7.9	Density of states [states/eV] illustrating the band gaps of SQS E and D with PBE and SCAN.	46
7.10	Density of states [states/eV] of SQS B with HSE06.	46
7.11	Pair distribution functions of SQS D (top) and B (bottom) . .	50
7.12	Contour plots of the Charge density of SQS A, B, D and E of $(\text{CrFeMnNi})\text{Si}_2$	51
7.13	CPU time of 48, 96 and 192-atom SQSs of $(\text{CrFeMnNi})\text{Si}_2$. . .	52
7.14	Density of states [states/eV] of SQS E 192 atom SQS.	54
7.15	Pair distribution functions of $(\text{CrFeMnNi})\text{Si}_2$ (top) 48-atom SQS, (middle) 96-atom SQS, (bottom) 192-atom SQS.	55
8.1	Projected density of states [states/eV] of (a) $\text{Cr}_3\text{Fe}_3\text{Mn}_7\text{Ni}_3\text{Si}_{32}$ (SQS B), (b) $\text{Cr}_5\text{Fe}_5\text{Mn}_3\text{Ni}_3\text{Si}_{32}$ (SQS C), (c) $\text{Cr}_5\text{Fe}_3\text{Mn}_5\text{Ni}_3\text{Si}_{32}$ (SQS A), (d) $\text{Cr}_3\text{Fe}_5\text{Mn}_5\text{Ni}_3\text{Si}_{32}$ (SQS D)	58
8.2	Projected density of states [states/eV] of $\text{Cr}_3\text{Fe}_3\text{Mn}_3\text{Ni}_7\text{Si}_{32}$ around E_F	59
8.3	Projected density of states [states/eV] of $(\text{CrFeMnCo})\text{Si}_2$. . .	63
8.4	Projected density of states [states/eV] of Co/Ti alloys based on the $(\text{CrFeMnNi})\text{Si}_2$ alloy.	63
8.5	Density of states [states/eV] of SQS A and E of $(\text{CoFeMnNi})\text{Si}_2$. .	64
A.1	Density of states SQS E $(\text{CrFeMnNi})\text{Si}_2$ with PBE.	70
A.2	Density of states SQS C $(\text{CrFeMnNi})\text{Si}_2$ with PBE. Nedos represent the number of points in the DOS calculation.	71
A.3	Density of states SQS C $\text{Cr}_5\text{Fe}_5\text{Mn}_3\text{Ni}_3\text{Si}_{32}$, illustrating the small finite DOS at E_F due to the impurity gap.	71
A.4	Projected density of states SQS A	72
A.5	Projected density of states SQS B	72
A.6	Projected density of states SQS E	73
A.7	Charge density of SQS C.	73

List of Tables

7.1	Total energy per atom (Toten), final magnetic moment per atom (Mag), band gap (E_G) and formation energy (E_{FPA}) of 5 SQS of $(\text{CrFeMnNi})\text{Si}_2$	37
7.2	Band gap of five SQSs of $(\text{CrFeMnNi})\text{Si}_2$ in spin up, down and total, calculated from the Kohn-Sham eigenvalues.	40
7.3	Band gap of SQS D as a function of occupancy cutoff in the eigenvalues.	41
7.4	Band gap of five supercells of $(\text{CrFeMnNi})\text{Si}_2$ calculated with PBE, SCAN and HSE06.	45
7.5	Minimum gap between k-point in valence band and conduction band in SQS B from PBE, SCAN and HSE06	47
7.6	Band gap from HSE06 calculations using Gaussian smearing, with smearing width σ equal to 0.05 eV and 0.005 eV, and the tetrahedron method (TBC). "-" means that the band gap are unchanged between $\text{occ} = 0.5$ and $\text{occ} = 0.01$	48
7.7	Total energy, magnetic moment and formation energy of 48, 96 and 192 atom SQSs of $(\text{CrFeMnNi})\text{Si}_2$	53
7.8	Band gap of SQSs of 48, 96 and 192-atoms of $(\text{CrFeMnNi})\text{Si}_2$. The names are arbitrary, A in 48 does not equal A in 96 or A in 192. The values listed in <i>italic</i> indicate a defect band gap. Structures listed in bold text represents the most stable supercell of the set of SQSs.	53
8.1	Total energy, magnetic moment and formation energy of various compositions of the Cr:Fe:Mn:Ni:Si system.	56
8.2	Band gaps of various compositions of $(\text{CrFeMnNi})\text{Si}_2$. Most stable SQS of a set is highlighted in bold text, defect/impurity band gap are listed in cursive. Some SQSs were excluded from the table due to unsuccessful calculations.	57
8.3	Total energy, magnetic moment and formation energy of various compositions of the $(\text{CrFeMnNi})\text{Si}_2$ alloy, where Cr, Mn, or Ni is replaced by Co/Ti.	61
8.4	Magnetic moment of the most stable SQS of different Co/Ti alloys based on the $(\text{CrFeMnNi})\text{Si}_2$ alloy.	61
8.5	The band gap in spin up/down and total of the most stable SQS of high-entropy silicides based on $\beta\text{-FeSi}_2$ with cobalt/titanium.	62

Acknowledgments

I would like to express my gratitude towards my supervisor Ole Martin Løvvik. For always being available and prioritize my work from the first day to the last. Coming into this project, I had no prior knowledge of density functional theory or quantum mechanical modeling. So, for your guidance in this project I am truly thankful, and know that this project would have been impossible without you. I also feel as if I have made a friend and someone I could talk through throughout this project. Due to the oddity of these recent years with the covid-19 outbreak and self-isolation this have been very important to my sanity and mental health combined with the difficulty involved in writing a master theses. On this same note, I would like to thank all my friends and family members that have been there and believed in me, and always reminding me to stay positive.

Chapter 1

Introduction

A major concern in the energy sector is the loss of energy as waste heat. An example of this is seen in for instance [1], where they estimated that about 60 percent of the energy produced in USA in 2012 was lost as waste heat. Contrary to most energy sources that suffer from this problem of losing energy to heat, thermoelectricity can generate electricity from heat by what's known as the Seebeck effect [2]. Thus, thermoelectricity have many promising applications, for example one could imagine a conjunction between thermoelectric generators and mechanical generators to recover a portion of the waste heat produced by the latter. However, currently thermoelectricity is of limited practical use due to a lack of efficient thermoelectric materials. This can be explained from the thermoelectric figure of merit, composed by the Seebeck Coefficient S , electrical conductivity σ , temperature T and the thermal conductivity, in the following relation [3]

$$zT = \frac{S^2\sigma T}{\kappa}. \quad (1.1)$$

Thus, an efficient thermoelectric material consist of three dependent factors: A high Seebeck coefficient, high electrical conductivity, and low thermal conductivity. A popular strategy to achieve this relation is the phonon-glass electron crystal approach [4], in which one will introduce complexity and anharmonicity to the crystal lattice by some means to increase levels of phonon scattering, without also increasing the scattering of electrons. Furthermore good thermoelectrics are narrow gap semiconductors, as explained in [5], that found the highest zT values for semiconductors with a band gap between $6\text{-}10 k_B T$, which at room temperature equals around 0.2 eV.

In this project we will look at high-entropy alloys as potential thermoelectric materials. High-entropy alloys are a novel material class that extends the concept of traditional binary-alloys such as steel, to multi-component alloys. The name "high-entropy" stems from the fact that mixing a larger number of elements increase the configurational entropy of the solution, that contribute to stabilize the materials. These materials are in particular known for their strong mechanical properties [6], for instance high strength at elevated temperatures. Furthermore evidence of

low thermal conductivity originating from a disordered crystal structure. Hence, provided that we can find narrow gap high-entropy alloys, these could be relevant and promising high zT thermoelectric materials.

Specifically, in this project we will look at high-entropy silicides. These are a lesser studied subclass of high-entropy alloys. The first experimentally synthesized high-entropy silicide was found in 2019 by Gild. et al [7]. He found a first of its kind single-phase high-entropy disilicide $(\text{MoNbTaW})\text{Si}_2$. This silicide adopted the hexagonal C40 crystal structure, and displayed low thermal conductivity compared to conventional disilicides in the equivalent crystal structure. Additionally, very recently a master thesis student at the University of Oslo managed to synthesize three phases of non-cubic high-entropy silicides based on Si, Co, Cr, Fe, and Ni in both hexagonal and orthorhombic symmetries [8]. We base this project on silicides because firstly silicon and various transition metal-silicides are environmentally sound and silicon in particular is heavily applied in micro-electronic devices and renewable energy sources such as solar power, thus silicon based alloys could readily be implemented into these technologies. Secondly, transition metal silicides offer a good range of initial compounds with suitable band gaps for thermoelectrics [9].

This project is performed by ab initio methods in the framework of density functional theory. The disordered structure of high-entropy alloys are handled with a numerical method called special quasi-random structures. The particular materials investigated in this project will be based on the semiconductor $\beta\text{-FeSi}_2$. We will mainly investigate the band gap of such alloys, for this we employ three classes of functionals in DFT: GGA, meta-GGA and hybrid functionals. In addition, we will perform a brief analysis of the stability and magnetism. The potential high-entropy silicides are studied by constructing five distinct supercells of the master compound, where the iron sites are populated by a quasi-random distribution between 3d transition metals. Special emphasis are placed on alloys consisting of Cr, Fe, Mn and Ni, as these along with silicon are sustainable non-toxic elements.

We begin this project by reviewing the fundamentals and properties of high-entropy alloys, thereafter we present a theoretical description of the computational methods in this project, SQS, and DFT. Next we discuss various practical aspects of DFT such as the exchange-correlation functionals and numerical convergence, in addition to numerical settings necessary to reproduce the results in this project. Finally we present and discuss the results, which begin with the high-entropy silicide $(\text{CrFeMnNi})\text{Si}_2$, followed by various derivatives and alternatives to this system. In the end we give a brief conclusion of our work and discuss possible directions for future research.

Part I

Theory

Part II

Method

Part III

Results and Discussion

Chapter 7

The high-entropy silicide $(\text{CrFeMnNi})\text{Si}_2$

7.1 $\beta\text{-FeSi}_2$

We begin with a brief overview of the master compound $\beta\text{-FeSi}_2$ that we have used as a foundation for the alloys in this project. In addition this is the sole case where our methods and results can be compared to experimental work and relevant literature.

$\beta\text{-FeSi}_2$ is a well known semiconductor with an experimentally measured band gap of around 0.85 eV at room temperature [10]. The nature of the band gap is under debate, although most ab initio studies result in an indirect gap, experimental studies agree on a direct band gap. From our own calculations we get an indirect band gap of 0.65 eV with the PBE GGA functional. In comparison, Materials Project lists a band gap of 0.70 eV with the same functional. This slight discrepancy is most likely down to use of different parameters in the calculations, for instance Materials project use a different pseudopotential with more valence electrons, and a larger cutoff energy of 520 eV. In agreement with Materials Project our calculations return a final magnetic moment of the compound equal to 0. This can be seen in the electronic density of states plotted in figure 7.1, by that the DOS and hence band gap are identical in both spin directions.

The formation energy E_{form} of the compound can be calculated as the difference in total energy between the product and the sum of reactants. For the FeSi_2 compound that consist of 16 iron atoms and 32 silicon we get

$$E_{\text{form}} = -327.72\text{eV} - (16 \times -8.32\text{eV} + 32 \times -5.42\text{eV}) = -21.16\text{eV},$$

or formation energy per atom $E_{FPA} = 0.441\text{eV}$ from $-21.16/48$. The total energy of iron and silicon were calculated separately for the respective base elements with identical parameters as used for the FeSi_2 calculation. The total energies correspond well with the listed energies from materials project of -8.4693 eV and -5.4234 eV for Fe, and Si respectively. Accordingly, the formation energy per atom for $\beta\text{-FeSi}_2$ of 0.441 eV is in good agreement with materials project's value of 0.444 eV.

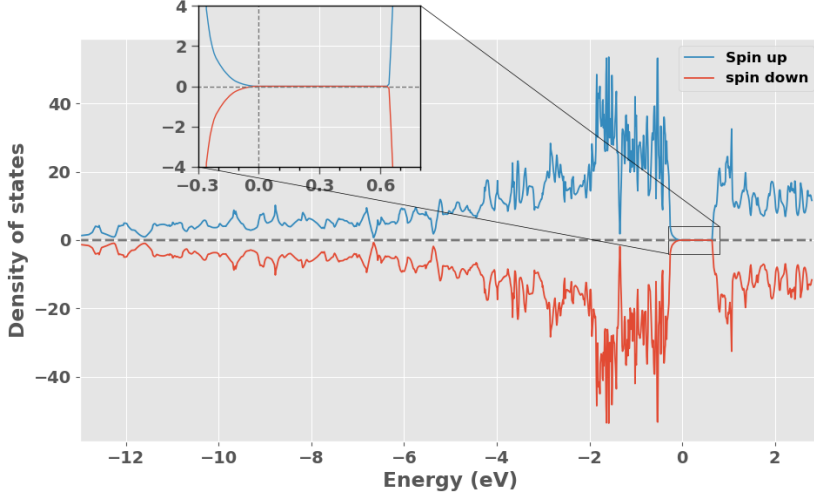


Figure 7.1: Density of states [states/eV] of $\beta\text{-FeSi}_2$.

7.2 $(\text{CrFeMnNi})\text{Si}_2$

The first alloy we will look at is the equimolar distribution of Cr, Fe, Mn and Ni. For details on this alloy, and a visualization of the supercells we refer the reader to section 6.2. Below in table 7.1 we list the total energy per atom, final magnetic moment per atom, and band gap of five distinct SQSs of the $\text{Cr}_4\text{Fe}_4\text{Mn}_4\text{Ni}_4\text{Si}_{32}$ alloy. In addition we include the mean and standard deviation (std) between the 5 supercells and the formation energy calculated from the mean total energy.

SQS	Toten (eV)	Mag (μ_B)	E_G (eV)
A	-6.608	0.083	0.028
B	-6.614	0.083	0.052
C	-6.606	0.083	0.034
D	-6.616	0.083	0
E	-6.609	0.083	0.050
Mean	-6.611	0.083	0.033
Std	0.004	0.000	0.021
E_{FPA} (eV)	-0.293	-	-

Table 7.1: Total energy per atom (Toten), final magnetic moment per atom (Mag), band gap (E_G) and formation energy (E_{FPA}) of 5 SQS of $(\text{CrFeMnNi})\text{Si}_2$.

From table 7.1 we observe that the total energy and magnetic moment are quite similar in all 5 supercells, which could be expected from that the only variable between supercells is the atomic configuration. On the other hand, the atomic configuration has a larger impact on the band gap of the

supercells. We find that the band gap ranges from a maximum value of 0.05 eV in SQS B, to a metal in SQS D, nevertheless much smaller than the band gap of 0.65 eV in FeSi₂. We will come back to the band gaps in section 7.2.1.

Contrary to the master compound, these supercells representing the (CrFeMnNi)Si₂ alloy, contain a finite magnetic moment of around 0.083 μ_B . However, compared to a ferromagnet such as iron, with Mag = 2.2 μ_B , according to Materials Project, we note that this is not a strong ferromagnetic alloy. The local magnetic moments show some variation between supercells, but follow the same trend where the largest moments are attributed to chromium atoms in the lattice, followed by manganese. On the other side the magnetic moments of both iron and nickel within the numerical accuracy of the calculations give negligible contributions to the magnetic moment of the structures. Considering that the total magnetic moment is identical in 5 distinct atomic configurations and the local magnetic moments show very similar trends, the observed magnetism within the scope of this project is most probably connected to the particular crystal structure. It should be noted however that the magnetic properties in this project could be prone to errors. As we discussed in section 4.3 one of the major drawbacks of DFT in regards to magnetic materials is the local minima problem. In this project we have overlooked this concern and applied a constant initial magnetic configuration to all structures, disregarding for example antiferromagnetic or possible permutations of ferrimagnetic orderings, to reduce the workload. Thus, it's possible that the final magnetic structure of the supercells adopts local minima rather than global. Coupling this with the possible errors associated with the special quasi-random structures method to model the disordered magnetic structure means that the magnetic results and following the total energy and corresponding stability are not immutable nor necessarily accurate in respect to the hypothetical real alloy.

In terms of the total energy the most and least stable SQSs are "D" and "A" respectively, meaning that SQS D is then the most representative configuration of the real material. However, most likely all five SQSs and other possible configurations would appear as local orderings in domains of the real material with a certain probability. Therefore we will consider and discuss the results of all 5 SQSs as well as the most stable supercell. Further, the total energy alone is not sufficient to evaluate the stability of the structure. In this project we have not considered factors such as the configurational entropy or made any finite temperature considerations. Additionally, the discussion above on the magnetic configuration could affect the total energy. Thus, the relative stability between supercells listed in table 7.1 could change. Nevertheless, we put the most effort into analyzing the most stable supercells of each alloy, as according to the considerations made in this project, are the most representative configurations of the real material.

7.2.1 The band gap

As seen from table 7.1, the band gap of the alloy is severely reduced from the master compound, and varies between supercell to supercell. We observed a maximum band gap of 0.05 eV in SQS B, and on the flip side a 0 band gap in the most stable configuration, SQS D. The density of states of SQS D and B are displayed in figures 7.2 and 7.3 below.

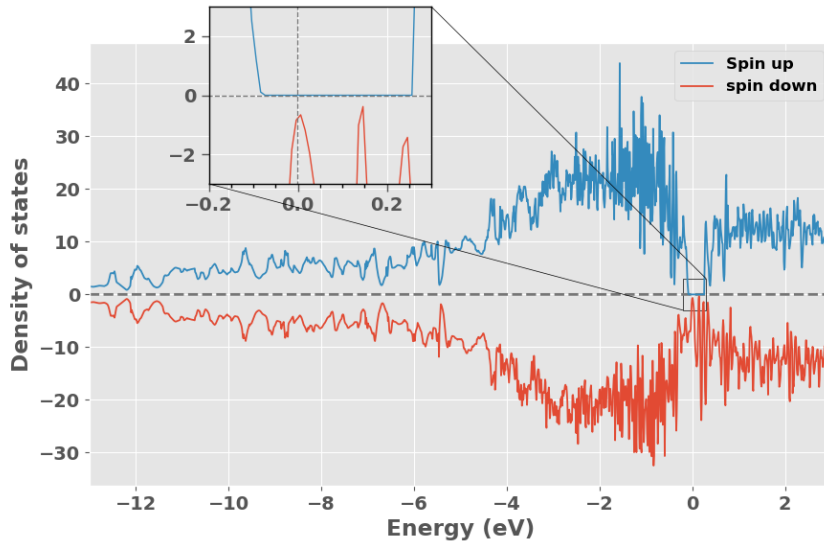


Figure 7.2: Density of states [states/eV] of SQS D of $(\text{CrFeMnNi})\text{Si}_2$.

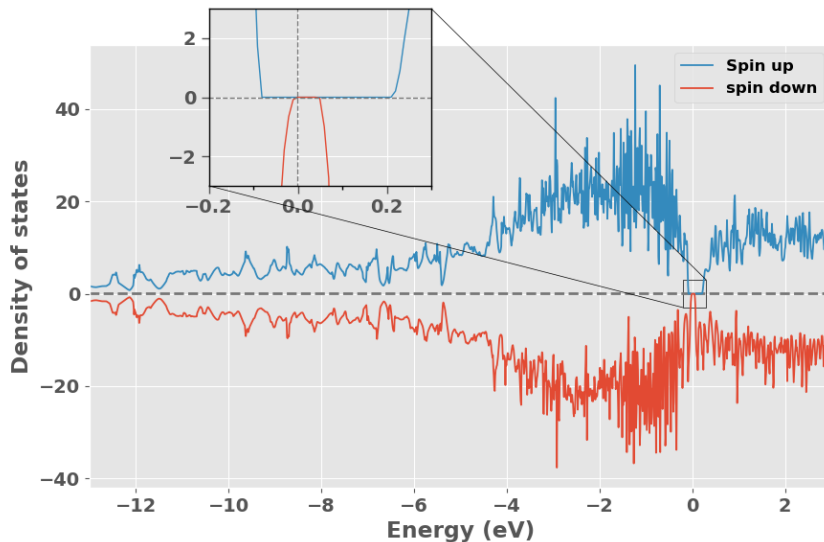


Figure 7.3: Density of states [states/eV] of SQS B of $(\text{CrFeMnNi})\text{Si}_2$.

In figure 7.2 and 7.3 we observe that the band gap in both SQS D and B, in accordance with the magnetic property differ between the spin

directions. Going forward we will refer to the band gap in spin up as E_G^{up} , and spin down as E_G^{dw} . Clearly in both D and B $E_G^{\text{up}} \gg E_G^{\text{dw}}$ as SQS D for instance exhibits a band gap of around 0.3 eV in spin up, contrary to a 0 in spin down. Comparing to the values in table 7.1 we find that the total band gaps of the respective structures are limited by the narrow or nonexistent band gap in spin down.

To obtain further and more precise information on the band gap we look to the calculated Kohn-Sham eigenvalues. The band gaps found from investigating the eigenvalues, denoted as E_G^{eigen} can be seen below in table 7.2 for all five SQS.

SQS	$E_G^{\text{up, eigen}}$ (eV)	$E_G^{\text{dw, eigen}}$ (eV)	$E_G^{\text{tot, eigen}}$ (eV)
A	0.081	0.052	0.028
B	0.293	0.052	0.052
C	0.236	0.034	0.034
D	0.340	0	0
E	0.310	0.050	0.050

Table 7.2: Band gap of five SQSs of $(\text{CrFeMnNi})\text{Si}_2$ in spin up, down and total, calculated from the Kohn-Sham eigenvalues.

Continuing the trend described above we observe equivalent to SQS D and B that $E_G^{\text{up}} \gg E_G^{\text{dw}}$ for all supercells, par SQS A. In this supercell the spin polarization of the band gap is damped, despite the supercell being equally magnetic to the other supercells. Moreover, in this case the total band gap $E_G^{\text{tot}} = E_G^{\text{up}} - E_G^{\text{dw}}$, as opposed to the other supercells where the total band gap is equal to the lesser spin down band gap of the structure. This can be seen in the density of states in figure 7.4. DOS plots of SQS C and E can be seen in appendix A.1, note that in SQS C we were required to increase the number of points to calculate the density of states (NEDOS in VASP) in order to observe the band gap.

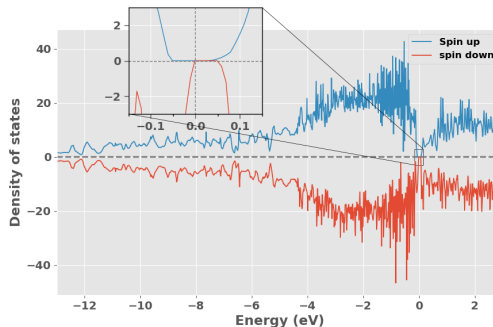


Figure 7.4: Density of states [states/eV] of SQS A of $(\text{CrFeMnNi})\text{Si}_2$.

In VASP the energy eigenvalues are listed for every energy band at all k-points used in the calculation, with corresponding occupancy. An

occupancy of 1 represents a fully occupied eigenstate, while a completely unoccupied (empty) eigenstate has occupancy equal to 0. We Recall that occupied states belong to the valence band, and the conduction band consists of unoccupied states (at 0 K). The highest energy valence band in these structures are band 124 in spin down and 128 in spin up, following the lowest energy valence band is 125/129 in spin down/up. The band gap in spin down is then determined from the difference between the lowest energy eigenvalue in band 125 and the highest energy eigenvalue in band 124, and likewise for the spin up band gap between bands 128 and 129. In SQS D different from the semiconducting structures we observe some partially occupied states at the band edges in bands 124 and 125 in spin down. With partially occupied states we refer to eigenstates in the valence band with occupancy less than 1 and states in the conduction band with occupancy above 0. Specifically, the highest energy eigenvalue (9.01 eV) in band 124 has occupancy equal to 0.94, and equivalently the lowest energy eigenvalue (8.98 eV) in band 125 has occupancy equal to 0.08. This results in a zero band gap. The Fermi energy of this structure is 8.99 eV, which means that the partially occupied eigenstate in band 124 is above the Fermi energy, and the partially unoccupied eigenstate in the conduction band below the Fermi energy. This is a clear indication of a metal, in which the conduction band and valence band overlap. In this project we will refer to such eigenstates with partial occupancy as defect states. The effect of the defect states on the band gap of SQS D can be seen in table 7.3. Here we calculate the band gap as a function of the defect states by an occupancy cutoff parameter occ , such that $E_G(0.99, 0.01)$ is the band gap when only including eigenvalues with occupancy above 0.99 in the valence band and below 0.01 in the conduction band. For simplicity we will write this parameter as a single value, where $occ = 0.01$ represents occupancy equal to 1 - 0.01 in the valence band and 0 + 0.01 in the conduction band.

occ	$E_G^{\text{up, eigen}}$ (eV)	$E_G^{\text{dw, eigen}}$ (eV)	$E_G^{\text{tot, eigen}}$ (eV)
0.5	0.340	0	0
0.05	0.340	0.021	0.021
0.01	0.340	0.050	0.050
0.001	0.340	0.073	0.073
<0.0001	0.340	0.086	0.086

Table 7.3: Band gap of SQS D as a function of occupancy cutoff in the eigenvalues.

From table 7.3 we find clear evidence of the defect states prohibiting the band gap in spin down in SQS D, compared to the semiconducting supercells that contain only fully occupied and unoccupied eigenstates. To investigate this effect to greater extent we compare the eigenvalues of SQS D to a pure metal, such as iron. In this case the energy bands (both spins) around the Fermi energy (5.8 eV) are populated mostly by partially

filled eigenstates. Inside a single energy band we observe instances of both more than half-filled states above E_F , and less than half-filled states above E_F , thus a clear overlap between the conduction and valence band. In contrast we find no instances of partial occupants in pure Si, as in the semiconducting SQSs. Therefore we can firmly state that the "defect states" are associated with a metallic character. Compared to the pure metal however, the amount and severity of the partial occupants are very damped in SQS D. The concept of defect or impurity states in the band gap has been found as a common feature of the band structure of random alloys [11], however we have reservations about if this is a physical result or related to numerical factors. In addition to partial occupants in Fe and SQS D we observe a plural of unphysical states where the occupancy exceeds 1 and 0. Recalling that the discontinues Fermi surface of metals poses several obstacles on DFT calculations with respect to the smearing and number of k-points. This result could then be imagined as a consequence of numerical methods. For instance in SQS B we conducted three separate electronic calculations, one with the tetrahedron method (value listed in tables) and two calculations with Gaussian smearing with smearing width 0.05 and 0.005 eV. With the Gaussian method and smearing width $\sigma = 0.05\text{eV}$ we get $E_G^{\text{up, eigen}} = 0.299\text{eV}$ and $E_G^{\text{dw, eigen}} = 0.050\text{eV}$. Further calculations with the Gaussian method with smearing width of 0.005 eV results in $E_G^{\text{up, eigen}} = 0.293\text{eV}$ and $E_G^{\text{dw, eigen}} = 0.052\text{eV}$. Compared to the values in table 7.3 with TBC, we observe that Gaussian (0.005 eV) and TBC are identical, while Gaussian (0.05 eV) show some deviation. Furthermore we find that the eigenvalues of Gaussian 0.05 eV contain defect states, and that the spin down band gap, as we experienced for SQS D, can be enlarged from $E_G^{\text{dw, eigen}}(0.01) = 0.170\text{eV}$. However, in this case we find no instances of non-naturalistic states as we described above for SQS D with TBC.

In conclusion, the defect states observed in SQS D appear to be related to a metallic structure, however from the discussion above we have seen that the results could be subject to numerical factors as well. It would have been instructive to visualize and analyze the eigenvalues by plotting the band structure. Unfortunately this is neither simple to perform or interpret for large supercells consisting of several elements and a large number of energy bands. One solution could be band-unfolding, but this did not work in conjunction with the implementation of the SQS method in this project.

7.2.2 Local and projected density of states

In this section we will analyze the local and projected density of states of primarily SQS D (most stable). Below we include the local density of states of silicon in figure 7.5, and the respective LDOS plots of the various 3d elements of the compound in figure 7.6.

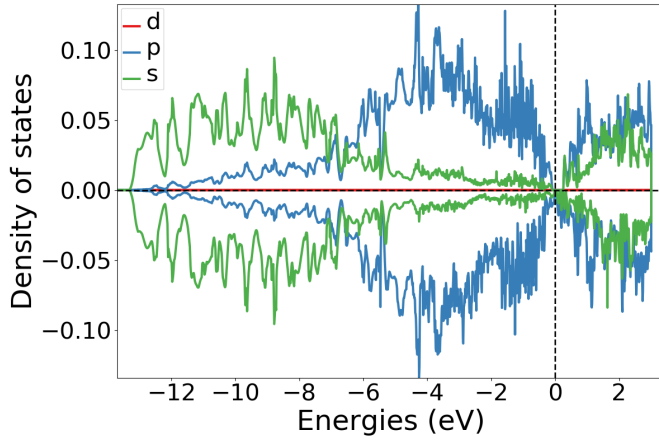


Figure 7.5: Local density of states [states/eV] of Si (SQS D)

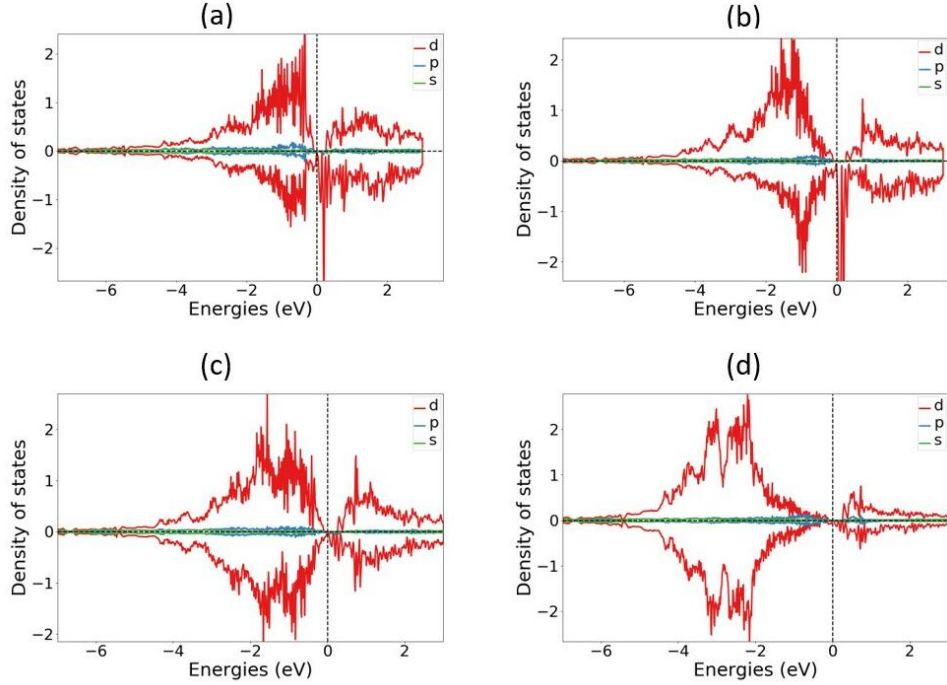


Figure 7.6: Local density of states [states/eV] of (a) Cr, (b) Mn, (c) Fe, (d) Ni in SQS D.

In the local density of states of Si we see that the s-electrons in Si occupy states in the lower energy regions and p electrons at slightly elevated energies closer to the Fermi energy. Above E_F states are occupied by s and p electrons equally. Between the 3d electrons of the transition metals, markedly manganese and chromium display a strong presence at energies just above E_F and manganese additionally below E_F . Iron and Nickel show largest contributions at energies further from the Fermi energy, most notably below E_F . In the spin up channel we see a similar trend where chromium lie closest to E_F followed by manganese, iron and lastly nickel

at the lowest energies. The interplay between the 3d elements and silicon can be seen from the projected density of states in figure 7.7.

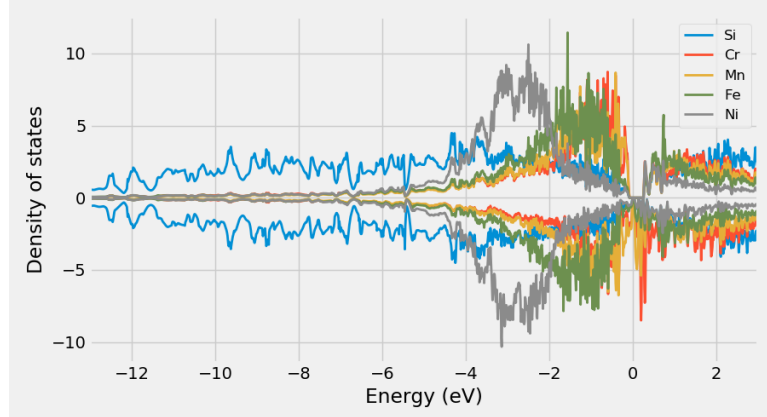


Figure 7.7: Projected density of states [states/eV] of SQS D.

Compared to bulk β -FeSi₂ [12], we observe good agreement of the local DOS of Fe and Si in this alloy. Moreover the relative positions are in good agreement with observed trends in simpler Si-rich 3d transition metal silicides [13]. In these compounds, the electronic structure tends to be dominated by d electrons, and the valence band density of states are filled by d states near E_F . The p-d hybridization between Si and TM elements is typically found at about 6 eV below E_F , and Si s states about 10 eV below. In our alloy we observe good agreement of s-electrons as seen in the local density of states in figure 7.5, but the p electrons are pushed up in energy closer to E_F .

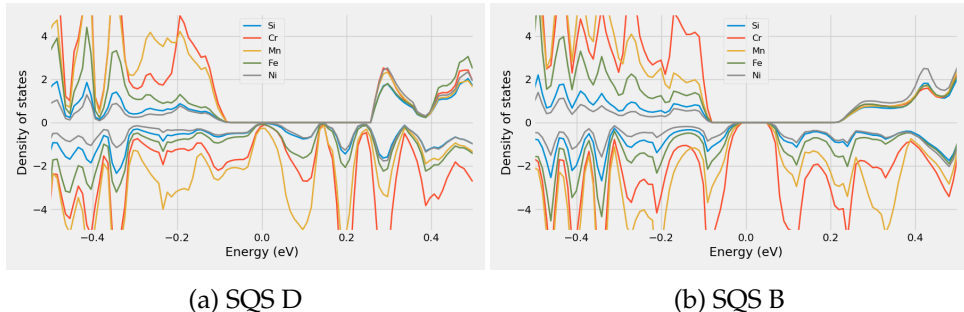


Figure 7.8: Projected density of states [states/eV] of SQS D and B around E_F .

In figure 7.8 above we have plotted the projected DOS of the half-metallic structure (SQS D) and the configuration with the largest E_G^{dw} (SQS B) around the Fermi energy. Compared to the semiconducting structure we can distinctly observe a large number of Mn states in SQS D around E_F , most noticeably in spin down, but also in spin up. The projected density of states of SQSs A, B, and E are included in appendix A.2 (unable to plot PDOS for SQS C).

7.2.3 The band gap with SCAN and HSE06

As expressed previously, in this work we invoke 3 steps of Jacob's ladder: GGA (PBE), meta-GGA (SCAN) and hybrid functional (HSE06), to determine the band gap. The outcome of these 3 functionals are showcased in table 7.4.

SQS	XC-functional	E_G^{up} (eV)	E_G^{dw} (eV)	E_G^{tot} (eV)
A	PBE	0.082	0.052	0.028
	SCAN	0	0	0
	HSE06	0.708	0.026	0.026
B	PBE	0.293	0.052	0.052
	SCAN	0.147	0.089	0.089
	HSE06	0.286	0.182	0.182
C	PBE	0.236	0.034	0.034
	SCAN	0.069	0.112	0.112
	HSE06	0.174	0.033	0.020
D	PBE	0.339	0	0
	SCAN	0	0.108	0
	HSE06	0.378	0	0
E	PBE	0.308	0.050	0.050
	SCAN	0.154	0.111	0.105
	HSE06	0.548	0.013	0.013

Table 7.4: Band gap of five supercells of $(\text{CrFeMnNi})\text{Si}_2$ calculated with PBE, SCAN and HSE06.

We will begin dissecting table 7.4 by comparing SCAN to PBE. The first distinction we make notice of is in SQS A. Here calculations with the SCAN functional predicts a metallic compound, contrary to the the PBE band gap of 0.03 eV. Alike the band gap of SQS D discussed previously, the 0 band gap in this structure with SCAN is caused by defect states. Neglecting such states and evaluating the band gap from exclusively almost completely filled and empty eigenstates yield $E_{G, \text{SCAN}}^{\text{up,eigen}}(0.01) = 0.032$ eV and $E_{G, \text{SCAN}}^{\text{dw,eigen}}(0.01) = 0.053$ eV, and a total band gap of 0.032 eV. This value seems to agree better with the PBE band gap of this supercell, but we observe that E_G^{up} is larger in PBE. This is a recurrent pattern with SCAN across all five SQSs, where $E_{G, \text{SCAN}}^{\text{up}} < E_{G, \text{PBE}}^{\text{up}}$, and moreover $E_{G, \text{SCAN}}^{\text{dw}} > E_{G, \text{PBE}}^{\text{dw}}$. This can be seen in figure 7.9, where we plot the density of states of SQS E (a, b) and C (c, d). Note that the SCAN band gap in SQS C has the opposite spin polarization of PBE; this is also the case in SQS D, as seen in table 7.4.

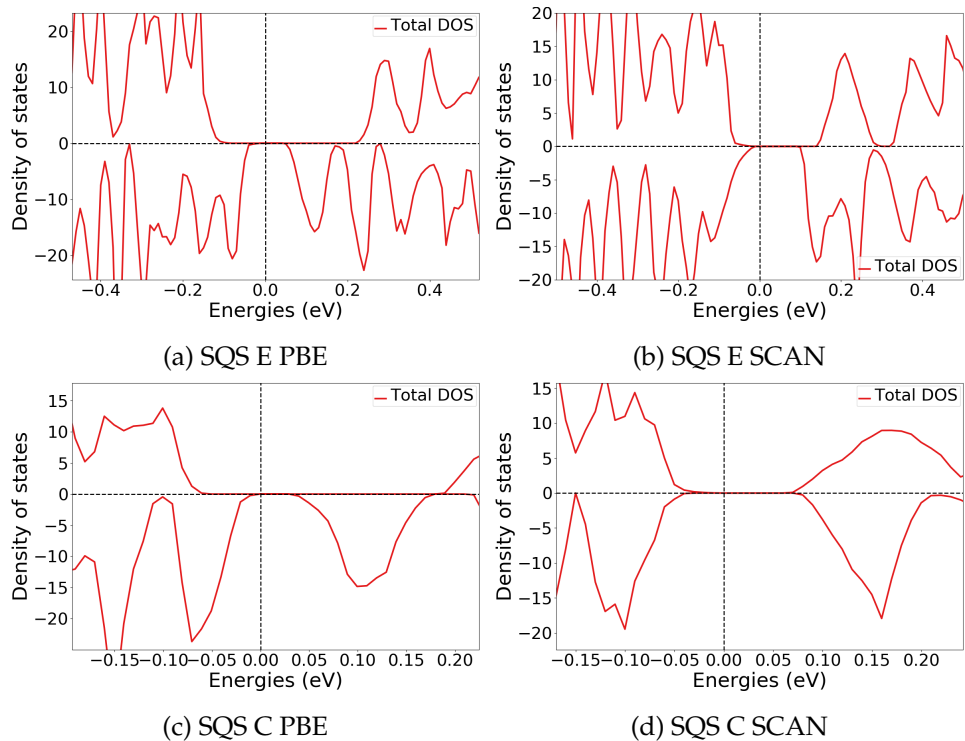


Figure 7.9: Density of states [states/eV] illustrating the band gaps of SQS E and D with PBE and SCAN.

With the HSE06 functional we observe the opposite trend in SQS A and E compared to SCAN, here $E_{G, \text{HSE06}}^{\text{up}} > E_{G, \text{PBE}}^{\text{up}}$ and $E_{G, \text{HSE06}}^{\text{dw}} < E_{G, \text{PBE}}^{\text{dw}}$. But in other cases $E_{G, \text{HSE06}}^{\text{up}}$ is lesser (SQS C) or similar to PBE (SQS B and D). On the other hand $E_{G, \text{HSE06}}^{\text{dw}}$ is consistently smaller in all structures compared to PBE, with the exception of SQS B. In this structure the HSE06 functional predicts large band gaps in both spin directions, this can be seen from the density of states plotted in figure 7.10.

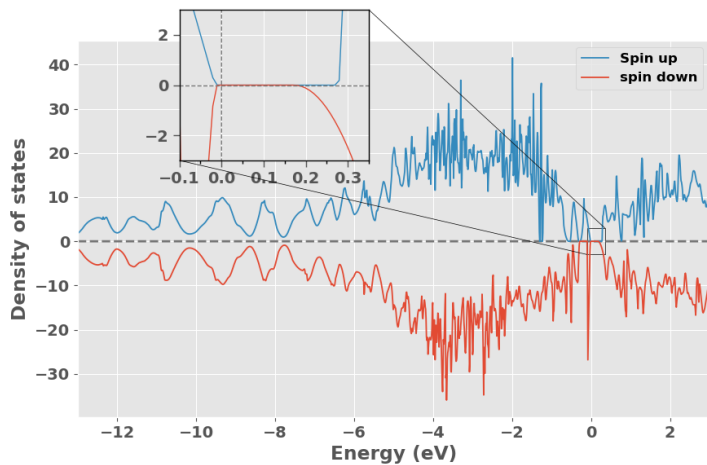


Figure 7.10: Density of states [states/eV] of SQS B with HSE06.

As we discussed in section 5.1, hybrid functionals are much more computationally demanding compared to both meta-GGA and GGA functionals. In this project we experienced particular difficulty of converging calculations with HSE06 of the compositionally complex SQSs. To reduce the cost of the HSE06 functional we performed such calculations with a lower density of k-points, see section 6.1. The small amount of k-points could as discussed lead to numerical inaccuracies relating to the calculation of the Fermi surface in metallic structures. Furthermore, the reduced mesh of k-points could result in artificially exaggerated band gaps from failing to encapsulate the exact minimum transition between the valence band and conduction band.

XC-functional	Transition (k-point)
PBE	$(1/4, 0, 1/4) \rightarrow (0, 0, 0)$
SCAN	$(1/4, 0, 1/4) \rightarrow (0, 1/3, 0)$
HSE06	$(1/2, 0, 0) \rightarrow (0, 0, 0)$

Table 7.5: Minimum gap between k-point in valence band and conduction band in SQS B from PBE, SCAN and HSE06

In table 7.5 we list the transition between the highest occupied k-state in the valence band and lowest unoccupied k-state in the conduction band for SQS B with PBE, SCAN and HSE06 respectively. We observe that all 3 functionals find different k-point transitions. A concerning factor is that the highest energy k-point in the valence band from PBE calculations $(1/4, 0, 1/4)$ is not included in the HSE06 calculation with the narrow mesh of $2 \times 2 \times 2$ k-points. Thus, one may suspect that the HSE06 calculation overlooks the minimum transition and hence returns an enlarged band gap instead. This could be the case in $E_{G,A}^{up}$ and $E_{G,B}^{dw}$ where HSE06 predicts much larger values than PBE. However, without an experimental baseline we can not conclude that this is the case. As in the other instances we find that HSE06 produces similar or lower band gaps compared to PBE despite of the smaller number of k-points.

As stated in section 6.2, we did not manage to converge the hybrid calculations using the tetrahedron method. We overcame this problem by first calculating the charge density using Gaussian smearing and utilizing the charge density to expedite TBC HSE06 calculations. The respective HSE06 band gaps of the five SQSs of the $(\text{CrFeMnNi})\text{Si}_2$ system from utilizing these methods are displayed in table 7.6. Here, the band gap is calculated from the eigenvalues at different cutoff occupancy occ to highlight the part of defect states. Gaussian smearing was tested with smearing width σ equal to 0.05 eV and 0.005 eV.

SQS	Smearing (type)	$E_G^{up,eigen}$ (0.5) (eV)	$E_G^{down,eigen}$ (0.5) (eV)	$E_G^{up,eigen}$ (0.01) (eV)	$E_G^{down,eigen}$ (0.01) (eV)	$E_G^{tot,eigen}$ (0.5) (eV)	$E_G^{tot,eigen}$ (0.01) (eV)
A	Gaussian (0.05)	0.784	0.149	-	0.298	0.149	0.298
	Gaussian (0.005)	0.212	0.101	-	-	0.101	-
	TBC	0.708	0.026	-	-	0.026	-
B	Gaussian (0.05)	0.278	0.170	0.299	0.314	0.151	0.298
	Gaussian (0.005)	0.284	0.182	-	-	0.180	-
	TBC	0.286	0.182	-	-	0.181	-
C	Gaussian (0.05)	0.108	0.106	0.241	0.184	0.065	0.184
	Gaussian (0.005)	0.130	0.022	-	-	0.022	-
	TBC	0.174	0.033	-	-	0.020	-
D	Gaussian (0.05)	0.366	0.059	-	0.187	0.059	0.187
	Gaussian (0.005)	0.374	0.072	-	-	0.072	-
	TBC	0.378	0	-	0.267	0	0.267
E	Gaussian (0.05)	0.665	0.144	-	0.168	0.144	0.168
	Gaussian (0.005)	0.583	0.121	-	-	0.121	-
	TBC	0.548	0.013	-	-	0.013	-

Table 7.6: Band gap from HSE06 calculations using Gaussian smearing, with smearing width σ equal to 0.05 eV and 0.005 eV, and the tetrahedron method (TBC). "-" means that the band gap are unchanged between $\text{occ} = 0.5$ and $\text{occ} = 0.01$.

As we experienced for SQS B (PBE) in section 7.2.1, defect states are only a factor in the calculations using Gaussian smearing with $\sigma = 0.05$ eV. These band gaps contain defect states, and can consequently be enlarged. By comparing E_G^{up} and E_G^{dw} at $occ = 0.5$ and $occ = 0.01$, the defects appear to have a lesser role in spin up, as per SQS C the band gap in spin up is either consistent or only marginally different between the defect band gap and the hypothetical defect less band gap. E_G^{dw} on the other hand, increases significantly by removing the defect states. The Gaussian smearing method is generally in better agreement with TBC at lower smearing width. But even in this case we observe several dissimilarities. In SQS A and E, E_G^{dw} is larger with the Gaussian method, additionally E_G^{up} is much lower in SQS A. Furthermore, while the HSE06 band gap in SQS D using TBC is in good agreement with PBE, where both results in a spin up half-metal. The HSE06 calculation of this SQS using Gaussian smearing, predicts a semiconductor with band gap equal to 0.07 eV with $\sigma = 0.005$ eV. In this project we have based our choice of numerical smearing on the advice on the VASP manual stating that for accurate total energies and density of states in semiconductors, one should opt for the tetrahedron method [14]. However, seeing as our system is comprised of metals in addition to Si, we include the results from utilizing Gaussian smearing. There are of course many more factors that affect the accuracy and reliability of both methods, but these are outside the scope of this project.

The fact that the majority of functionals and SQS agree on the presence of a band gap is in itself an overwhelmingly positive result, that allow us to state with high certainty that the potential high-entropy silicide $(\text{CrFeMnNi})\text{Si}_2$ is in fact a semiconductor, or possibly a half-metal based on the observed spin polarization and the most stable configuration. Regarding the 3 functionals applied in this project, we experience best cohesion between PBE and HSE06 that both agree on a spin up polarization of the band gap, while SCAN predicts more symmetric band gaps. This can also be seen from the magnetic moment, whereas PBE and HSE06 yields a final magnetic moment (per atom) of $0.083 \mu_B$ across all SQSs, with SCAN this is reduced to half the amount. In the nonmagnetic $\beta\text{-FeSi}_2$ structure we find better agreement between PBE and SCAN. Both correctly predicts that the material is nonmagnetic, however compared to the experimental value of about 0.85 eV and the PBE band gap of 0.65 eV, we get a smaller band gap of 0.61 eV with SCAN. Thus, the SCAN functional does not necessarily result in increased accuracy over PBE, even in the simpler nonmagnetic structure. To conclude this section on the band gap of the $(\text{CrFeMnNi})\text{Si}_2$ alloy, when studying the band gap with DFT, particularly PBE is well known to underestimate the band gap of the real material as we experienced for FeSi_2 . Therefore, a band gap found with PBE indicates the existence of a band gap of at least the same size of the real material. In the following sections, we will heavily emphasize the PBE functional to determine the band gap from both the fast and reliable use in addition to the points mentioned above. Furthermore, from our experiences in this project in conjunction with the lack of support, the SCAN function looks to perform quite poorly with respect to band gaps. The HSE06 functional on

the other hand, yielded much more reliable results, however since it was often computationally expensive and troublesome to implement for the structures in this project, we apply this scarcely in proceeding sections.

7.2.4 Pair distribution functions

The pair distribution functions of SQS D and B are included below in figure 7.11. We compare the PDFs of the most stable configuration (SQS D) with those of SQS B to investigate distinctions between the half-metallic structure and the most stable semiconducting configuration (SQS B).

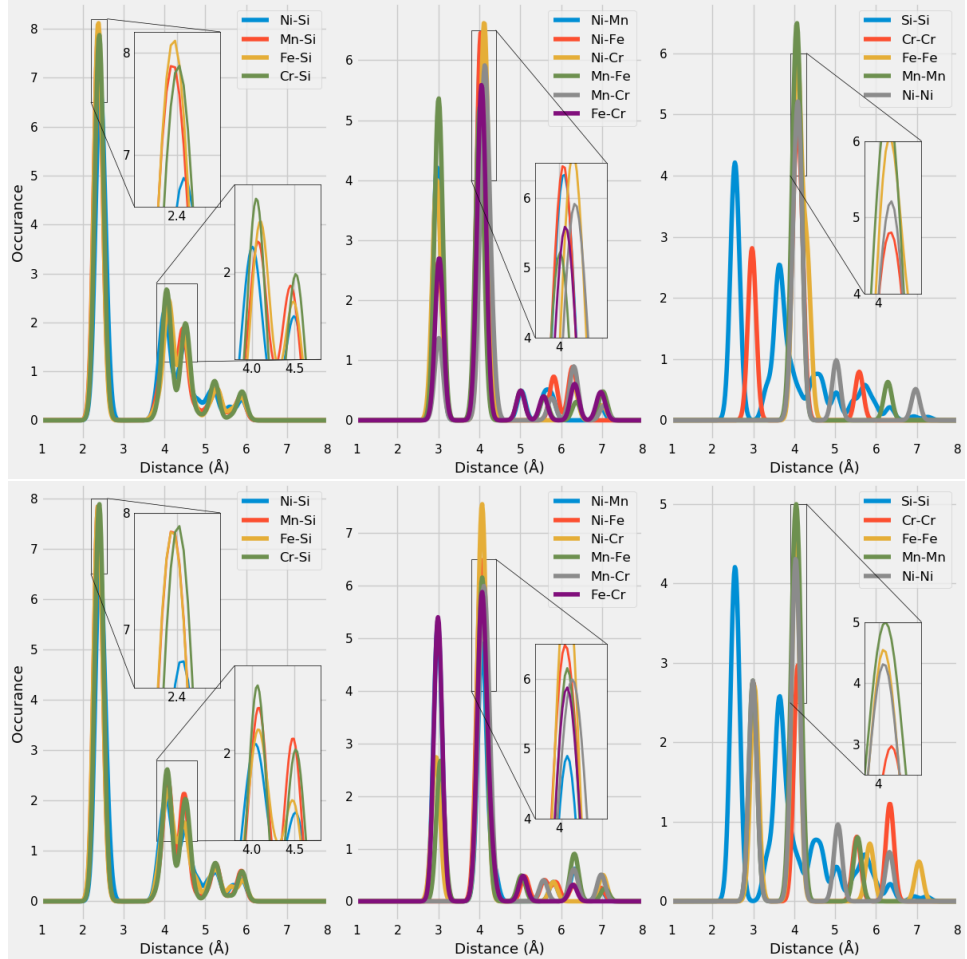


Figure 7.11: Pair distribution functions of SQS D (top) and B (bottom)

With the aid of the ICSD [15], we can compare the PDFs in figure 7.11 to a compilation of PDFs based on a large number of experimental compounds. As these SQSs contains a total of 15 different bonds, comparing each one to the ICSD values would be an exhaustive process. According to the ICSD, the preferred bond-length of TM-Si bonds is observed at two values, with the shorter length the most occurring. Specifically Fe-Si bonds range between 2.25-2.75 Å and 4-5 Å, Mn-Si between 2.25-2.75 Å and 3.5-5 Å, Ni-Si between 2.25-2.5 Å and 3.85-5 Å, and

finally Cr-Si between 2.35-2.65 Å and 4-5 Å. Clearly, the PDFs of the SQSs are in good agreement with the listed values of TM-Si bonds. The relative occurrence of the bonds between SQS D and B are mostly consistent, other than marginally reduced Fe-Si occurrence at 2.4 Å in B.

Nevertheless, we observe several differences between TM-TM bonds in SQS D and B, such as Mn-Fe, Cr-Fe, and Ni-Mn bonds. This is simply a consequence of how the SQSs are generated; the silicon atoms are placed as before in the new supercells, but the TM elements are quasi-randomly distributed. Thus, it's reasonable that we would find the major differences between TM-TM bonds. Recalling that manganese in particular had a distinct presence in spin down around E_F in SQS D, we observe that this particular supercell compared to SQS B has a preference of Mn-Fe bonds at 3 Å compared to Fe-Cr in SQS B, and overall larger preference of Mn-Mn bonds. However, the differences between PDFs are difficult to relate to the observed properties. Firstly because of the sheer number of total bonds to analyze, and secondly considering the uniqueness of each SQS.

7.2.5 Charge density

Below we include the calculated charge density with PBE of SQS A, B, D and E of the $(\text{CrFeMnNi})\text{Si}_2$ alloy. We note that the half-metallic configuration (SQS D) appears to contain a marginally larger number of delocalized electronic charges in the lattice ,compared to the semiconducting SQSs. The charge density of SQS C is found in appendix A.3.

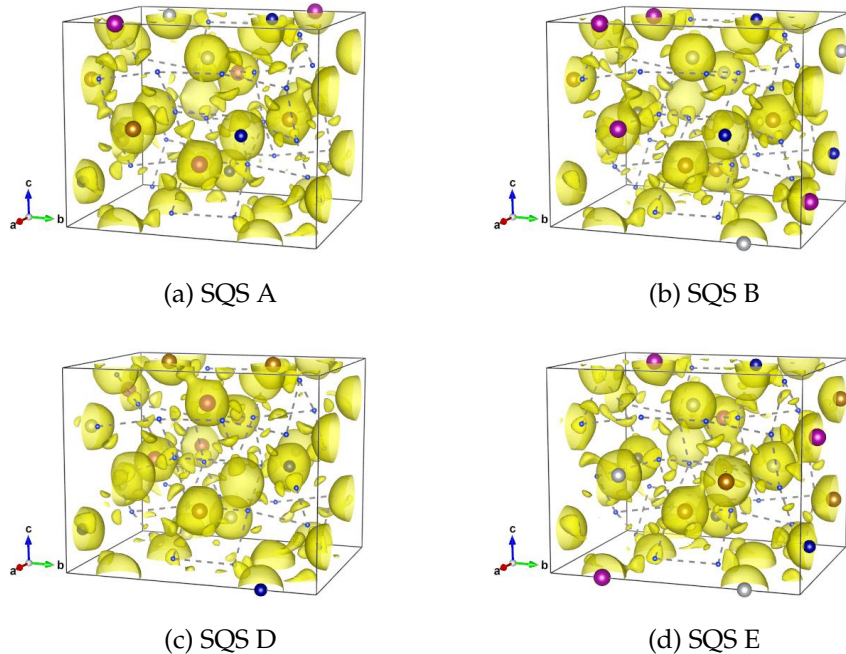


Figure 7.12: Contour plots of the Charge density of SQS A, B, D and E of $(\text{CrFeMnNi})\text{Si}_2$.

7.2.6 SQS size

Above we have presented the results of a high-entropy silicide $(\text{CrFeMnNi})\text{Si}_2$, investigated by five 48-atom SQSs with a volume of 700 \AA^3 . This intermediate size allowed for more computationally affordable computations, and enabled us to calculate the band gap by more complex and expensive functionals, moreover test different settings, computational factors and compositions. However, as we discussed in section 4.3, the application of the SQS method to HEAs is not necessarily straightforward. The most pressing concern is the size of the SQS model and if it's sufficient enough to correctly model the disordered multi-component structure. In this section we will investigate factors of the SQS-method on the band gap and related results, by studying the difference between the 48 atom SQSs discussed above, to that of 96 and 192-atom SQSs with volumes 1200 \AA^3 and 2400 \AA^3 respectively. The computational cost of the 3 models are displayed below in figure 7.13 in terms of the number of CPU hours for both geometric and electronic relaxation of the structures.

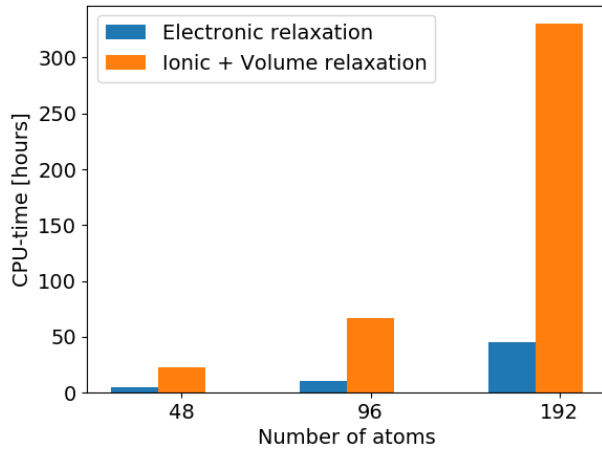


Figure 7.13: CPU time of 48, 96 and 192-atom SQSs of $(\text{CrFeMnNi})\text{Si}_2$

like the 48-atom model, the 96 and 192-atom SQS were tested by five unique configurations. In table 7.7 we list the mean and standard deviation from the set of configurations for all three sizes, with respect to the total energy per atom and final magnetic moment per atom, in addition to the formation energy of the mean total energy. Clearly, the 3 properties show minimal variation between the three sizes, furthermore we do not observe any indication of convergence with respect to the size. Thus, we may state that the 48-atom SQSs is sufficient for these materials. On the other hand, we observe that the larger models contain larger deviation between configurations, this can be expected given the increased total number of atoms that can vary between configurations.

SQS size	Toten (eV)		Mag (μ_B)		E_{FPA} (eV)
	mean	std	mean	std	
48 atoms	- 6.611	0.004	0.083	0.000	-0.292
96 atoms	- 6.609	0.002	0.071	0.011	-0.292
192 atoms	- 6.612	0.002	0.076	0.017	-0.295

Table 7.7: Total energy, magnetic moment and formation energy of 48, 96 and 192 atom SQSs of $(\text{CrFeMnNi})\text{Si}_2$

The band gap corresponding to SQSs of each size are listed in table 7.8. First and foremost the band gap is evident in all three and exhibits analogous spin polarization, however appears to be less frequent and smaller in the larger structures. This result could simply be related to the uniqueness of each SQS, as also in the larger SQSs we observe sizable band gaps in certain configuration. Additionally, the larger cells has an increased possibility to create defect states.

SQS size	SQS	$E_G^{up,eigen}(0.5)$ (eV)	$E_G^{dw,eigen}(0.5)$ (eV)	$E_G^{tot,eigen}(0.5)$ (eV)
48 atoms	A	0.082	0.052	0.028
	B	0.293	0.052	0.052
	C	0.236	0.034	0.034
	D	0.339	0	0
	E	0.308	0.050	0.050
96 atoms	A	0.171	0.044	0.037
	B	0.139	0.027	0.027
	C	0.135	0.036	0.008
	D	0.089	0.040	0.040
	E	0.161	0	0
192 atoms	A	0.120	0.032	0.032
	B	0.144	0	0
	C	0.187	0	0
	D	0.048	0.034	0
	E	0.013	0.018	0.013

Table 7.8: Band gap of SQSs of 48, 96 and 192-atoms of $(\text{CrFeMnNi})\text{Si}_2$. The names are arbitrary, A in 48 does not equal A in 96 or A in 192. The values listed in *italic* indicate a defect band gap. Structures listed in bold text represents the most stable supercell of the set of SQSs.

Equivalent to structure D in the 48 atom SQS, we find that the 0 band gap in SQS E in the 96 atom model suffers from defect states, without defects we find $E_G^{dw,eigen}(0.01) = 0.016$ eV. The same is true for SQS B and C (192), but require $occ = 0.001$ to yield a small finite value. The

band gap in SQS D and E (192) on the other hand, is finite at $occ = 0.5$, but can be enlarged from increasing occ , as we described for calculations utilizing Gaussian smearing with $\sigma = 0.05$ eV. Specially, In SQS D (192-atoms), $E_G^{up,eigen}(0.01) = 0.075$ eV and $E_G^{dw,eigen}(0.01) = 0.05$ eV, similarly $E_G^{up,eigen}(0.01) = 0.05$ eV, and $E_G^{dw,eigen}(0.01) = 0.048$ eV in SQS E (192-atoms). In such cases where the eigenvalues inclusive of defect states return a finite band gap, the density of states does not. This is seen in figure 7.14 for SQS E in the 192-atom model that clearly has nonzero DOS at E_F in both spin direction.

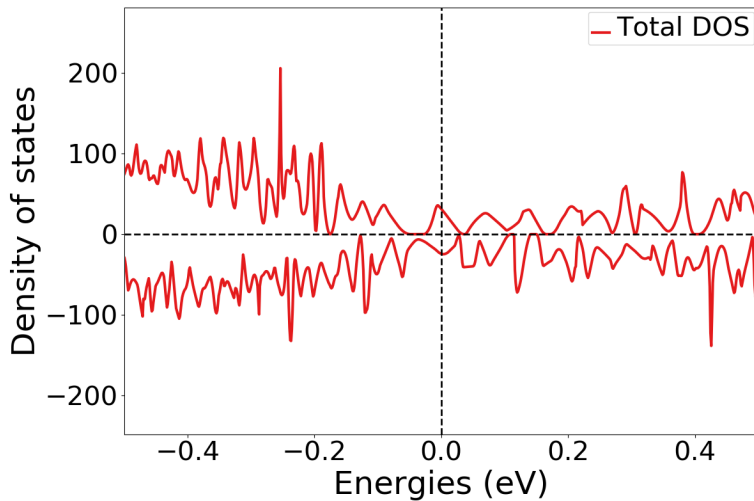


Figure 7.14: Density of states [states/eV] of SQS E 192 atom SQS.

One could wonder if the very narrow band gap in SQS E (192) of 0.013 eV is subject to numerical precision in the DOS. But on the grounds of the small value we calculated the DOS in this case by 20000 points over the energy range -12 eV to 12 eV, which results in a resolution of about 8 points per 0.01 eV. In other words this should not be a factor.

Drawing any conclusion on the band gaps is difficult seeing as we find very different results within all 3 sizes. The most stable SQSs suggests that the band gap converge towards a small or possible non-existent band gap with increasing SQS size. On the other hand we also find evidence of large band gaps in the larger cells in less stable configurations. This goes back to section 3.3 where we mentioned that one particular difficulty of the SQS method is the large number of possible atomic configurations of one compositions.

Looking at the pair distribution functions of the most stable SQS in each model (figure 7.15), we observe that short-range interactions is well represented and identical across all three models. The distinctions between preferences as discussed in section 7.2.4 are most likely a product of the uniqueness of the SQSs more so than the size. On the other hand, the larger SQSs clearly provide a better description of long-range interactions that is not nearly as present in the smaller supercell. But, as seen from the minimal

variation of the values in table 7.7 between the 3 models, in accordance with the fundamental philosophy of the SQS method, the functional properties are determined primarily from short-range interactions in the lattice. Thus, despite the fact that the larger SQSs offer improvements over the smaller SQSs, the gain is not justified by the increased computational cost.

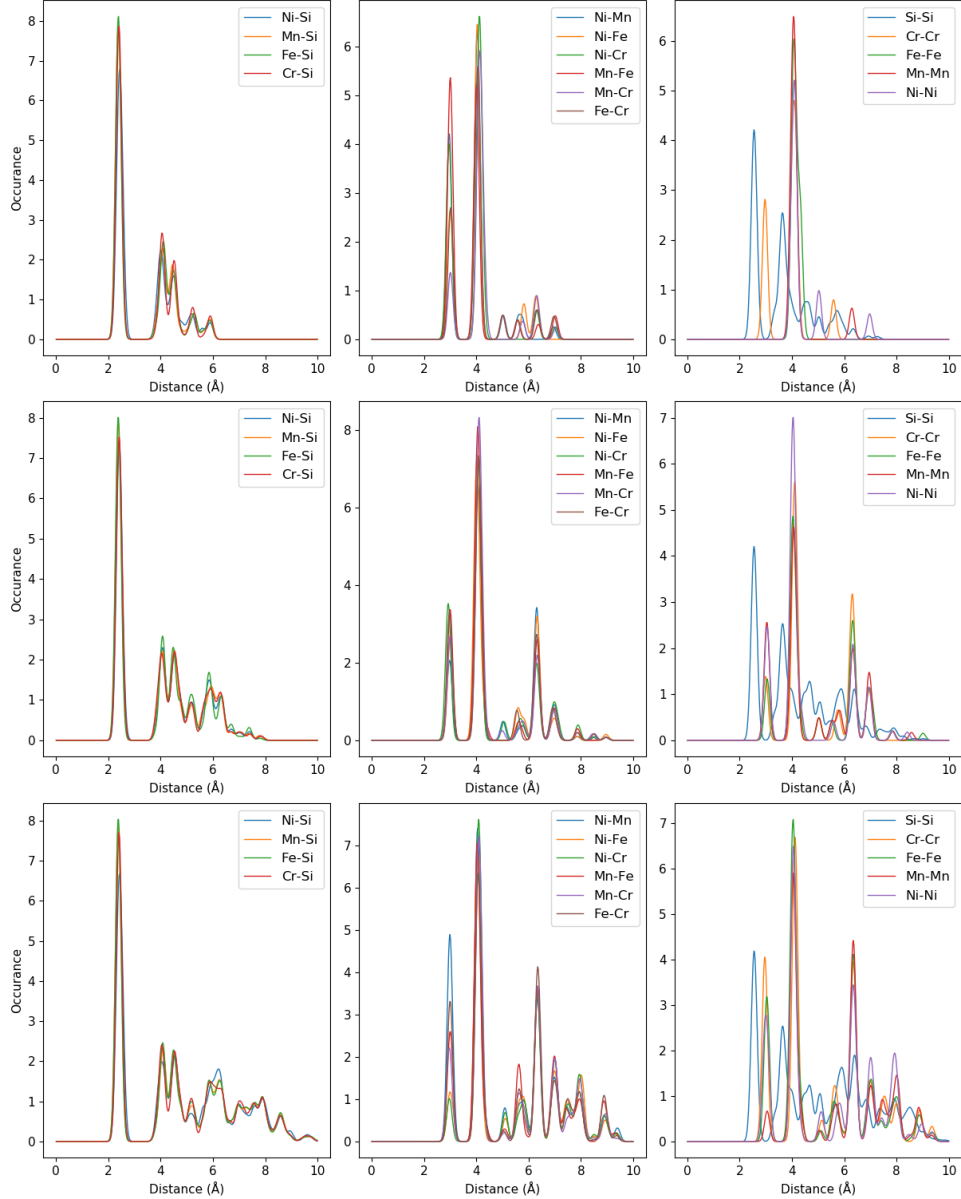


Figure 7.15: Pair distribution functions of $(\text{CrFeMnNi})\text{Si}_2$ (top) 48-atom SQS, (middle) 96-atom SQS, (bottom) 192-atom SQS.

Chapter 8

Alternative compositions

Up until this point we have looked in detail at the high-entropy silicide $(\text{CrFeMnNi})\text{Si}_2$. In this chapter we will broaden our search of compositions based on the β - FeSi_2 structure. First, we will look at various compositions inside the quaternary phase diagram of Cr, Fe, Mn and Ni, then consider some compositions where chromium, manganese or nickel are replaced by cobalt or titanium.

8.1 Exploring the quaternary phase diagram

In this section, we aim to expand our search of this diagram by generating SQSs of the 48 atom model slightly away from equimolar distribution of 3d elements. The list of compositions are listed in table 8.1, with corresponding total energy, magnetic moment and formation energy in the familiar format. Ideally each composition would differ only by one element to provide a clear view of each direction in the phase diagram, but the TDEP implementation insisted in also reducing Nickel to stay consistent with the 48 atom supercell.

Composition	Toten (eV)		Mag (μ_B)		E_{FPA} (eV)
	mean	std	mean	std	
$\text{Cr}_3\text{Fe}_3\text{Mn}_7\text{Ni}_3\text{Si}_{32}$	- 6.695	0.004	0.138	0.019	-0.300
$\text{Cr}_5\text{Fe}_5\text{Mn}_3\text{Ni}_3\text{Si}_{32}$	- 6.671	0.003	0.113	0.022	-0.286
$\text{Cr}_5\text{Fe}_3\text{Mn}_5\text{Ni}_3\text{Si}_{32}$	- 6.685	0.004	0.138	0.046	-0.271
$\text{Cr}_3\text{Fe}_5\text{Mn}_5\text{Ni}_3\text{Si}_{32}$	- 6.680	0.004	0.094	0.021	-0.315
$\text{Cr}_3\text{Fe}_3\text{Mn}_3\text{Ni}_7\text{Si}_{32}$	- 6.392	0.008	0.016	0.010	-0.285

Table 8.1: Total energy, magnetic moment and formation energy of various compositions of the Cr:Fe:Mn:Ni:Si system.

In table 8.1 we observe that moving away from the equimolar system result in both less and more stable alloys. Clearly the lowest formation energies (most stable) correspond to compositions rich in manganese

and poor in chromium. Likewise the least stable compositions in table 8.1 contain either increased amounts of Cr or reduced amounts of Mn compared to the equimolar system. In the equimolar composition the magnetic moment was attributed to primarily Cr and Mn atoms in the lattice. In table 8.1 we observe similarly that compositions rich in Cr and Mn exhibits the largest magnetic moments and vice versa. The band gaps of the respective compositions in five unique SQSs can be seen in table 8.2 below, calculated with PBE GGA.

Composition	SQS	$E_G^{\text{up, eigen}}(0.5)$ (eV)	$E_G^{\text{dw, eigen}}(0.5)$ (eV)	$E_G^{\text{tot, eigen}}(0.5)$ (eV)
$\text{Cr}_3\text{Fe}_3\text{Mn}_7\text{Ni}_3\text{Si}_{32}$	A	0.339	0	0
	B	0.475	0	0
	C	0.134	0	0
	D	0.195	0.006	0.006
	E	0.421	0	0
$\text{Cr}_5\text{Fe}_5\text{Mn}_3\text{Ni}_3\text{Si}_{32}$	A	0.003	0	0
	C	0.210	0	0
	D	0.067	0.041	0.037
	E	0.362	0	0
$\text{Cr}_5\text{Fe}_3\text{Mn}_5\text{Ni}_3\text{Si}_{32}$	A	0.208	0	0
	B	0.405	0	0
	C	0.466	0	0
	D	0.084	0.012	0.012
	E	0.301	0	0
$\text{Cr}_3\text{Fe}_5\text{Mn}_5\text{Ni}_3\text{Si}_{32}$	A	0.392	0	0
	C	0.129	0	0
	D	0.260	0.100	0.100
	E	0.359	0.100	0.085
$\text{Cr}_3\text{Fe}_3\text{Mn}_3\text{Ni}_7\text{Si}_{32}$	A	0	0	0
	B	0	0	0
	C	0	0	0
	D	0	0	0
	E	0.040	0	0

Table 8.2: Band gaps of various compositions of $(\text{CrFeMnNi})\text{Si}_2$. Most stable SQS of a set is highlighted in bold text, defect/impurity band gap are listed in cursive. Some SQSs were excluded from the table due to unsuccessful calculations.

From table 8.2 we observe that most compositions are half-metals like the equimolar system with a spin up polarization. Each composition shows large variation between configurations. We note $E_{G,\text{max}}^{\text{up}} \approx 0.5$ eV and $E_{G,\text{min}}^{\text{up}} \approx 0.1$ eV in both $\text{Cr}_3\text{Fe}_3\text{Mn}_7\text{Ni}_3\text{Si}_{32}$ and $\text{Cr}_5\text{Fe}_3\text{Mn}_5\text{Ni}_3\text{Si}_{32}$, and further $E_{G,\text{max}}^{\text{up}} \approx 0.4$ eV and $E_{G,\text{min}}^{\text{up}} \approx 0.1$ eV in $\text{Cr}_3\text{FeMn}_5\text{Ni}_3\text{Si}_{32}$. In all three

of these compositions the proportion of manganese is increased relative to the equimolar system, and two out of the three compositions contain reduced amounts of chromium. Looking at the two compositions with the least indication of a band gap $\text{Cr}_5\text{Fe}_5\text{Mn}_3\text{Ni}_3\text{Si}_{32}$ and $\text{Cr}_3\text{Fe}_3\text{Mn}_3\text{Ni}_7$, these contain reduced amounts of manganese. Thus, based on the few compositions tested in this experiment we can state a relation of the band gap mainly to manganese, but also chromium.

Based on the most stable configuration of each composition, we observe very encouraging results in the $\text{Cr}_3\text{Fe}_3\text{Mn}_7\text{Ni}_3\text{Si}_{32}$ composition with the largest E_G^{up} of the set of configurations. Likewise the most stable SQS of the $\text{Cr}_3\text{Fe}_5\text{Mn}_5\text{Ni}_3\text{Si}_{32}$ composition is a semiconductor with a total band gap of about 0.1 eV. In the composition $\text{Cr}_5\text{Fe}_5\text{Mn}_3\text{Ni}_3\text{Si}_{32}$, the most stable SQS predicts a defect or impurity band gap as we discussed previously where the eigenvalues return a finite band gap despite of defect states. However we have not been able to investigate the nature and effect of this impurity band gap to further extent, likewise for the similar impurity gaps listed in table 8.2 and the 0 band gaps in spin down. Below in figures 8.1 and 8.2 we include the projected density of states around E_F of the most stable SQS of each composition. Because we only include and discuss the most stable SQS, the features of these figures can be subject to the uniqueness of that particular SQS rather than a distinct feature of the exact composition, however as stated previously the most stable configuration provides the most likely properties of the composition within the scope of this project.

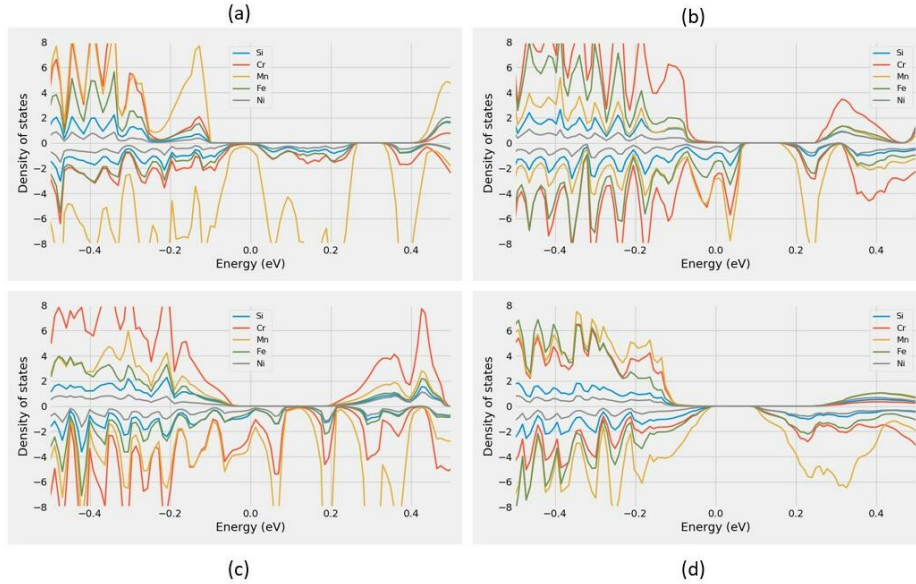


Figure 8.1: Projected density of states [states/eV] of (a) $\text{Cr}_3\text{Fe}_3\text{Mn}_7\text{Ni}_3\text{Si}_{32}$ (SQS B), (b) $\text{Cr}_5\text{Fe}_5\text{Mn}_3\text{Ni}_3\text{Si}_{32}$ (SQS C), (c) $\text{Cr}_5\text{Fe}_3\text{Mn}_5\text{Ni}_3\text{Si}_{32}$ (SQS A), (d) $\text{Cr}_3\text{Fe}_5\text{Mn}_5\text{Ni}_3\text{Si}_{32}$ (SQS D)

The PDOs is in good agreement with the listed values in table 7.2. $\text{Cr}_3\text{Fe}_3\text{Mn}_7\text{Ni}_3\text{Si}_{32}$ and $\text{Cr}_5\text{Fe}_3\text{Mn}_5\text{Ni}_3\text{Si}_{32}$ both display sizable band gaps in

spin, while figure 8.1 d point to a total band gap around 0.1 eV for SQS D of $\text{Cr}_3\text{Fe}_5\text{Mn}_5\text{Ni}_3\text{Si}_{32}$. On the other hand we observe as for the 192-atom SQS a dissimilarity between the density of states band gap in $\text{Cr}_5\text{Fe}_5\text{Mn}_3\text{Ni}_3\text{Si}_{32}$ SQS C (figure 8.1 b) and the eigenvalue (impurity) band gap listed in table 7.2. This can be better understood by figure A.3 in appendix A.1 that clearly show small finite values at E_F in spin up. This DOS may resemble that of a doped material.

In figure 7.7 we observed that manganese distinctly occupied states in the spin down channel around E_F and was a key contributor as to why the spin down channel of $(\text{CrFeMnNi})\text{Si}_2$ was metallic in the most stable SQS. This is also largely the case in the compositions shown above in figure 8.1 and 8.2, and is particularly evident in figure 8.1 where Mn dominate the spin down states around E_F in the $\text{Cr}_3\text{Fe}_3\text{Mn}_7\text{Ni}_3\text{Si}_{32}$ composition. By reducing the number of Mn we still find that the Mn states prohibit the band gap in spin down, as seen in figure 8.1 b. In the chromium rich compositions plotted in figures 8.1 b and c, we observe that also Cr states prohibit the spin down band gap, and dominate states near E_F in spin up as well. Contrary, in the $\text{Cr}_3\text{Fe}_3\text{Mn}_3\text{Ni}_7\text{Si}_{32}$ composition plotted in figure 8.2, we do not observe any distinct peaks of elements, but rather consistent small finite DOS around E_F in all elements. The sole composition with clear evidence of a spin down gap is from the chromium poor system plotted in figure 8.1 d. Also in this structure we see that the effects of Mn around E_F is dominant in spin down from the relative large amounts of Mn, but in comparison to the other composition these states are pushed away from the Fermi energy.

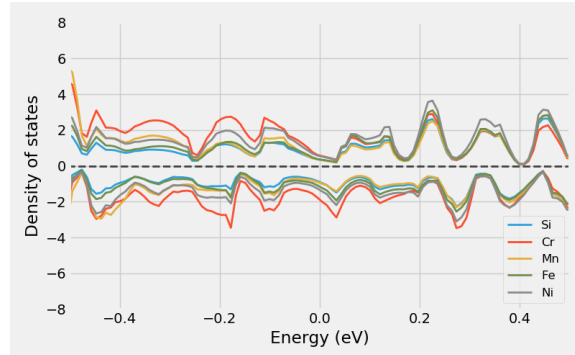


Figure 8.2: Projected density of states [states/eV] of $\text{Cr}_3\text{Fe}_3\text{Mn}_3\text{Ni}_7\text{Si}_{32}$ around E_F

An important factor of these results is that because each composition alters simultaneous elements, interpreting and relating the results to a particular alteration is challenging. For example, is the result of the $\text{Cr}_5\text{Fe}_3\text{Mn}_5\text{Ni}_3\text{Si}_{32}$ permutation a consequence of less Fe or increments to both Cr and Mn? Furthermore is the large band gap in spin up of $\text{Cr}_3\text{Fe}_3\text{Mn}_7\text{Ni}_3\text{Si}_{32}$ a product of increasing manganese or reducing the other elements. From the comparatively large gaps in spin up of $\text{Cr}_3\text{Fe}_3\text{Mn}_7\text{Ni}_3\text{Si}_{32}$ and $\text{Cr}_3\text{Fe}_5\text{Mn}_5\text{Ni}_3\text{Si}_{32}$ and the more present Cr states in

spin up in the Cr rich permutations we here conclude that the band gap is related to lessening of chromium, more so than other effects. However we see from both $\text{Cr}_5\text{Fe}_5\text{Mn}_4\text{Ni}_3\text{Si}_{32}$ and $\text{Cr}_3\text{Fe}_3\text{Mn}_3\text{Ni}_7\text{Si}_{32}$ (figure 8.2) in addition to the manganese rich composition that Mn plays a vital role on the band gap of these structures. It's clear that the $\text{Cr}_3\text{Fe}_5\text{Mn}_5\text{Ni}_3\text{Si}_{32}$ alloy manage to strike a balance between 3d elements that results in a specific interplay and correspondingly very promising properties. It would have been beneficiary to look at for example the pair distribution functions and compare to the equimolar system, but from the factors discussed in section 7.2.4 we leave this to future work.

As stated before, we have relied on the PBE GGA functional to determine the band gap in this part from its reliability and favorable computation cost. However, we have conducted calculations with SCAN and HSE06 on some of the more promising structures. For instance in SQS D of $\text{Cr}_3\text{Fe}_5\text{Mn}_5\text{Ni}_3\text{Si}_{32}$ we get lower values in both spin up and down with SCAN, specifically $E_{G,\text{SCAN}}^{\text{up}} = 0.21 \text{ eV}$ and $E_{G,\text{SCAN}}^{\text{dw}} = 0.08 \text{ eV}$. On the other hand HSE06 predicts $E_{G,\text{HSE06}}^{\text{up}} = 0.53 \text{ eV}$ and $E_{G,\text{HSE06}}^{\text{dw}} = 0 \text{ eV}$. In SQS B of $\text{Cr}_3\text{Fe}_3\text{Mn}_7\text{Ni}_3\text{Si}_{32}$ we observe very different outcomes. With SCAN we get a small band gap in spin down of about 0.002 eV and 0 in spin up, likewise the HSE06 band gap of this structure is $E_{G,\text{HSE06}}^{\text{up}} = 0.08 \text{ eV}$ and $E_{G,\text{HSE06}}^{\text{dw}} = 0.11 \text{ eV}$, opposed to $E_{G,\text{PBE}}^{\text{up}} = 0.47 \text{ eV}$ and $E_{G,\text{PBE}}^{\text{dw}} = 0 \text{ eV}$. Further the HSE06 band gap is in fact an impurity band gap, with $E_{G,\text{HSE06}}^{\text{up,eigen}}(0.01) = 0.18 \text{ eV}$ and $E_{G,\text{HSE06}}^{\text{dw,eigen}}(0.01) = 0.16 \text{ eV}$.

8.2 High entropy silicides with cobalt/titanium

The compositions we have tested in this section are deliberate combinations intended to both investigate the role of individual elements in the $(\text{CrFeMnNi})\text{Si}_2$ system, and broaden our search of potential high-entropy silicides based on $\beta\text{-FeSi}_2$. The compositions introduce Co/Ti at the cost of Cr, Mn and Ni. Note that the alloys contain a total of 48 atoms as before.

In similar fashion to the preceding section, we begin by presenting the new high-entropy silicides by the mean and standard deviation of the total energy and magnetization of 5 unique SQSs of each alloy, in table 8.3.

In terms of the formation energy, we observe that cobalt evidently yield the utmost stable alloys from the tested compositions, with $(\text{CoFeMnNi})\text{Si}_2$ at the top and $(\text{CrFeCoNi})\text{Si}_2$ at the bottom. On the other side, both $(\text{CrFeTiNi})\text{Si}_2$ and $(\text{CrFeMnTi})\text{Si}_2$ where we introduce titanium in place of manganese and nickel respectively, result in the overall least stable compositions. A precise physical interpretation of the stability between compositions is challenging from the shallow analysis in this project, but we do note that the two most stable alloys consist of the most chemically similar elements with respect to properties such as the electronegativity and atomic size. Following the least stable alloys are comprised of the most chemically dissimilar elements. This is in good agreement with the discussion in section 2.2 regarding phase formation of high-entropy alloys. Additionally, in the compositions discussed in the previous section we

found that the most stable composition was $\text{Cr}_3\text{Fe}_5\text{Mn}_5\text{Ni}_3\text{Si}_{32}$ where the Cr proportion was lessened. In conjunction with the results of the titanium we thus may suspect that smaller elements are ill-suited in this structure.

Composition	Toten (eV)		Mag (μ_B)		E_{FPA} (eV)
	mean	std	mean	std	
$\text{Cr}_4\text{Fe}_4\text{Co}_4\text{Ni}_4\text{Si}_{32}$	- 6.466	0.006	0.008	0.016	-0.308
$\text{Co}_4\text{Fe}_4\text{Mn}_4\text{Ni}_4\text{Si}_{32}$	- 6.473	0.005	0.000	0.000	-0.355
$\text{Cr}_4\text{Fe}_4\text{Ti}_4\text{Ni}_4\text{Si}_{32}$	- 6.422	0.009	0.031	0.029	-0.209
$\text{Cr}_4\text{Fe}_4\text{Mn}_4\text{Ti}_4\text{Si}_{32}$	-6.699	0.007	0.114	0.064	-0.199
$\text{Cr}_4\text{Fe}_4\text{Mn}_4\text{Co}_4\text{Si}_{32}$	-6.769	0.003	0.133	0.033	-0.323

Table 8.3: Total energy, magnetic moment and formation energy of various compositions of the $(\text{CrFeMnNi})\text{Si}_2$ alloy, where Cr, Mn, or Ni is replaced by Co/Ti.

In line with the other compositions studied in this project, the magnetization is clearly related to chromium and manganese also in this case. This is seen by the overall lowest magnetic moments in the two compositions without these elements, and reversely the highest magnetic moments is found for compositions with both Cr and Mn. Comparing the magnetic moment of $(\text{CrFeCoNi})\text{Si}_2$ and $(\text{CoFeMnNi})\text{Si}_2$ it seems in our study that chromium is most responsible for the magnetic moment in these alloys. Furthermore we find that substituting Ni with both Ti and Co yields more magnetic compounds. As we have discussed previously, the uniqueness of each SQS makes it difficult to draw conclusion on the various properties. In table 8.4 below we list the magnetic moment of the utmost stable SQS in each alloy. Contrary to the mean value we find that $(\text{CrFeCoNi})\text{Si}_2$ equal to $(\text{CoFeMnNi})\text{Si}_2$ is nonmagnetic, moreover $(\text{CrFeMnTi})\text{Si}_2$ are less magnetic relative to both $(\text{CrFeMnCo})\text{Si}_2$ and $(\text{CrFeMnNi})\text{Si}_2$.

Composition	Magnetic moment (μ_B)
$\text{Cr}_4\text{Fe}_4\text{Co}_4\text{Ni}_4\text{Si}_{32}$	0
$\text{Co}_4\text{Fe}_4\text{Mn}_4\text{Ni}_4\text{Si}_{32}$	0
$\text{Cr}_4\text{Fe}_4\text{Ti}_4\text{Ni}_4\text{Si}_{32}$	0,065
$\text{Cr}_4\text{Fe}_4\text{Mn}_4\text{Ti}_4\text{Si}_{32}$	0,079
$\text{Cr}_4\text{Fe}_4\text{Mn}_4\text{Co}_4\text{Si}_{32}$	0,167

Table 8.4: Magnetic moment of the most stable SQS of different Co/Ti alloys based on the $(\text{CrFeMnNi})\text{Si}_2$ alloy.

Thus, based on the utmost stable configurations we can state that replacing either Cr or Mn (with Co), removes the magnetic moment of the

alloy. Furthermore we find that the magnetic moment is reduced when Ni is substituted with Ti, and increased by Co. However, while substituting manganese with Co yields a nonmagnetic alloy, Ti for Mn only slightly reduces the magnetic moment.

In regards to the band gap, we find most to be metals. In table 8.5 we list the band gap of the most stable SQS of each composition, where the band gap is determined from the eigenvalues at different occupancy cutoff occ values to underline the effect of defect states. We find that increasing the criteria, in other words only consider states with occupancy above a certain threshold, the band gap become finite with $occ = 0.1$ and converge to around $0.02 - 0.06$ eV depending on composition at $occ = 0.01$.

Composition	occ	$E_G^{\text{up, eigen}}$ (eV)	$E_G^{\text{dw, eigen}}$ (eV)	$E_G^{\text{tot, eigen}}$ (eV)
CrFeCoNiSi_2	0.5	0	0	0
	0.1	0.001	0.040	0.001
	0.01	0.063	0.063	0.063
CrFeTiNiSi_2	0.5	0.007	0	0
	0.1	0.061	0.009	0.009
	0.01	0.061	0.037	0.037
CoFeMnNiSi_2	0.5	0	0	0
	0.1	0.004	0.004	0.004
	0.01	0.027	0.027	0.027
CrFeMnTiSi_2	0.5	0	0	0
	0.1	0.021	0.001	0
	0.01	0.030	0.030	0.022
CrFeMnCoSi_2	0.5	0.461	0	0
	0.1	0.607	0.022	0.022
	0.01	0.607	0.025	0.025

Table 8.5: The band gap in spin up/down and total of the most stable SQS of high-entropy silicides based on $\beta\text{-FeSi}_2$ with cobalt/titanium.

Contrary to the metallic or very narrow gap alloys, the CrFeMnCoSi_2 composition exhibits a band gap of around 0.5 eV in spin up. In figure 8.3 we plot the projected density of states of this structure. As was generally the case for the Cr:Fe:Mn:Ni:Si alloys, this structure displays a dominant number of manganese states in spin down at energies just above E_F , and large number of Cr states right below E_F in spin up. Analog to the most stable supercell of the $\text{Cr}_5\text{Fe}_5\text{Mn}_3\text{Ni}_3\text{Si}_{32}$ alloy discussed in section 8.1, the presence of defect states in the spin up band gap of CrFeMnCoSi_2 results in small finite DOS at the Fermi energy, and the band gap calculated from the eigenvalues is shifted above E_F , resembling that of a doped material.

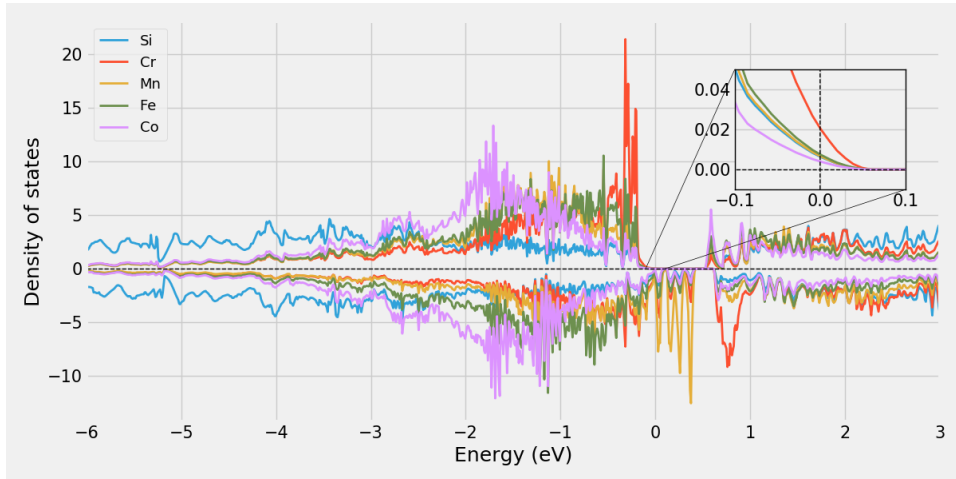


Figure 8.3: Projected density of states [states/eV] of $(\text{CrFeMnCo})\text{Si}_2$.

The PDOs of the other four alloys is displayed in figure 8.4. In agreement with the values listed in table 8.5, we observe from the PDOS that these are metallic compounds with finite DOS at E_F in both spins.

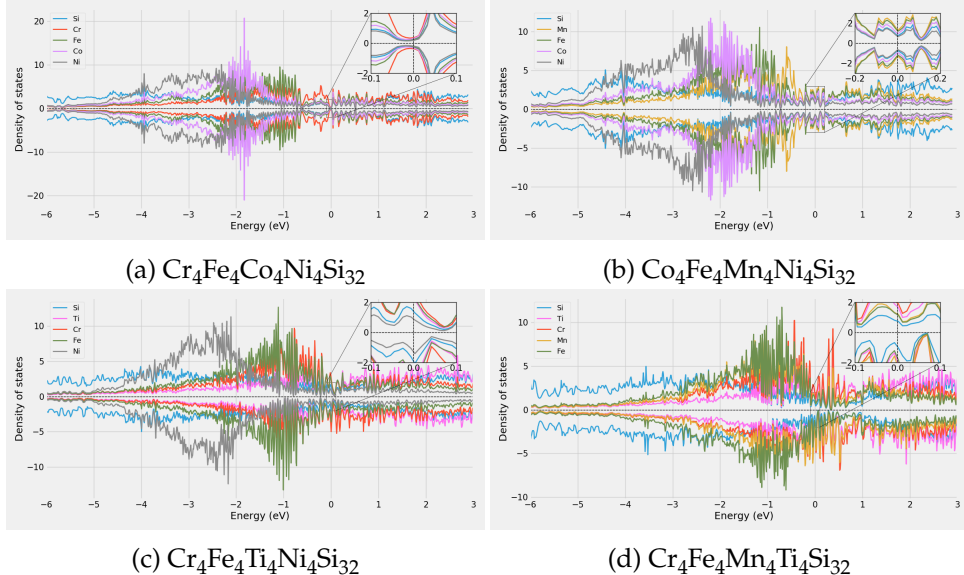


Figure 8.4: Projected density of states [states/eV] of Co/Ti alloys based on the $(\text{CrFeMnNi})\text{Si}_2$ alloy.

Above we have evaluated the band gap of the different alloys based on the most stable configuration. Across all five configurations we find that the band gap is more or less consistent in $(\text{CrFeCoNi})\text{Si}_2$, (CrFeMnTiSi_2) , $(\text{CrFeTiNi})\text{Si}_2$ and $(\text{CrFeMnCo})\text{Si}_2$. The most interesting case is the CoFeMnNiSi_2 alloy, here we observed very narrow total band gaps in two lesser stable configurations (SQS A and E) of 0.03 eV and 0.006 eV respectively. The density of states of these structures are displayed in figure 8.5.

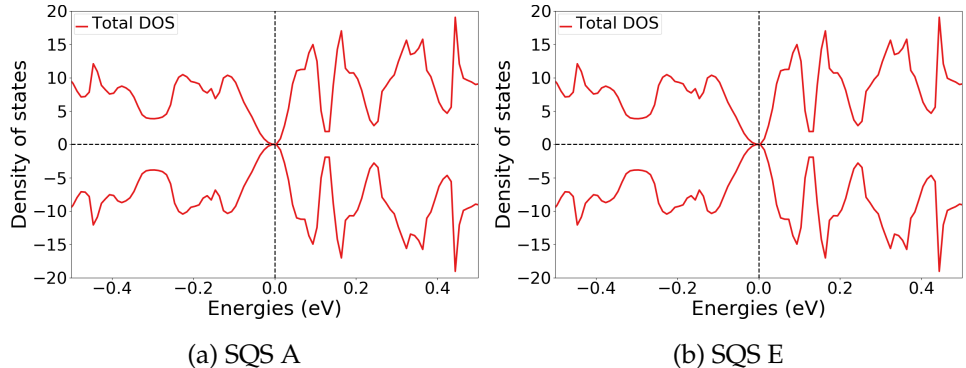


Figure 8.5: Density of states [states/eV] of SQS A and E of $(\text{CoFeMnNi})\text{Si}_2$.

8.3 Negative systems

In the above sections we have observed that aside from the $(\text{CrFeMnNi})\text{Si}_2$ alloy, we experience limited success in locating semiconducting compounds, particularly when moving away from the Cr:Fe:Mn:Ni:Si system. In addition to compounds discussed above, we have performed simulations of computations of

In addition to the compounds discussed above, we attempted to replicate the CrFeMnNi system based on other silicides, such as hexagonal CrSi_2 , trigonal Fe_2Si , and tetragonal and orthorombic Mn_4Si_7 , but found no indication of a band gap in these alloys. Furthermore we have tested a few alloys consisting of Sc, V, Zn, and Cu as well, but found no band gaps in these compositions either.

CrSi_2

From our calculations with PBE DFT we find the bulk $\text{crsi}2$ material to be an indirect semiconductor with a band gap of 0.33 eV, slightly below the listed value of 0.36 eV in materials project [cite](#), surprisingly we find a smaller gap of 0.32 eV from the SCAN functional. The compound is also nonmagnetic in agreement with materials project. For the bulk material we employed a 9 atom cell, with 6 silicon and 3 cr atoms, from this we generated SQSs of 72 atoms with the same ratio. **Include toten per atom for the unit cell? and figure of SQS + unit cell?**. For this given composition and system we observe very similar results to that of the compositions discussed above, the eigenvalues of several SQSs report a small band gap, but it's not apparent from either the density of states or from the bandgap.py script of pymatgen. Additionally, we can not reproduce the gap with the SCAN functional, as was possible for the CFMN ($\text{fesi}2$) system.

MnSi

In the tetragonal configuration, the bulk material is a nonmagnetic indirect semiconductor with a band gap of 0.76 eV according to our PBE calculations, and 0.78 eV from SCAN. Materials project find a band gap of 0.76 eV, in good agreement with our own PBE results. The unit cell consists of 44 total atoms, 16 manganese and 28 silicon. In the orthoromibic cell,

with equal number of elements we find a band gap of 0.76 eV (0.77 ev SCAN) as well. In contrast, the CFMN alloy of both these cells produce metallic compounds. It should be noted that structures B and D in the tetragonal system did not fully relax, same for D in the orthorombic cell, so these results could be inaccurate.

Fe2Si

In this cell, we drastically alter the metal-silicon ratio, this is seen both in the band gap and magnetic properties of the material. The magnetic moment of this cell consisting of 4 iron atoms and 2 silicon atoms is 0.67, from the iron atoms. This magnetic character can also be observed from the discrepancy between the two spin channels. In spin down we find a band gap of 0.21 eV, while there is no gap in spin up. This gap can also be seen in the density of states **Include figure**. This however is an abnormal result in regard to other experimental work and literature on the Fe2Si cite https://www.sciencedirect.com/science/article/pii/S0925838816329796?casa_token=g9DRpu9IClcAAAAA:6Gd12A4Kh9J2igUWMVwHN8OSIKzD27VACA052FNsSAWhRY6PE Our results are subject to errors, particularly we note that the eigenvalues used to calculate the gap contain nonphysical values in the spin down channel. However, the gap is evident in the density of states thus we include the result in this report, but acknowledge the uncertainties revolving the value.

From this unit cell we generate 54 atom SQSs. From table .. we see that the magnetic nature remains, producing the overall highest magnetic moment of all studied supercells, which is not a surprising result considering the 3d metal to silicon ratio. **More on magnetic and total energy.** The magnetism can also be seen in the difference between the two spin channels, the bands where the occupancy transition from 1 to 0, ie occupied to not occupied is very different. In the most magnetic supercell D, we saw a distance of 22 bands between the spin down transition and spin up transition. Most supercells are metals from our PBE calculations. B and D show a very small gap of around 0.01 eV in one spin channel. In E we find a very narrow gap semiconductor with a total gap of 0.002 eV. This gap is surrounded by the same uncertainties as discussed previously.

Part IV

Conclusion and future work

Chapter 9

Conclusion

High-entropy alloys has emerged as a rapidly growing interest in materials science from the large range of possibilities and flexibility. In this project we have set out to study the possibility of a narrow gap semiconducting high-entropy silicide with top of the line computational power and methods, in the prospect of discovering next-generation efficient thermoelectric materials. The materials in mind were based on the FeSi_2 semiconductor, and modeled with the SQS method in the framework of DFT. To study the potential semiconductors we generated five distinct configurations of each composition and investigated the band gap, mainly with PBE GGA.

Our most successful effort was based around a 48-atom model of chromium, iron, manganese, and nickel in the Cr:Fe:Mn:Ni:Si system. In the equimolar composition $(\text{CrFeMnNi})\text{Si}_2$, we observed large variation of the band gap between the five distinct configurations. In spin up, the band gap ranged from 0.08 - 0.34 eV. The most stable supercell was a half-metal, while the other four supercells displayed small spin down gaps between 0.03 eV and 0.05 eV as well. Calculations with SCAN and HSE06 produced unpredictable outputs that varied greatly between SQSs, and contained a larger degree of uncertainty compared to PBE. However, with HSE06 we found spin up band gaps of 0.55 eV and 0.71 eV in two respective supercells, and a total band gap of 0.18 eV in another. Contrary, the SCAN functional resulted in total band gaps around 0.1 in three SQSs, one metallic supercell and one half-metallic structure with a spin down band gap of 0.1 eV.

Following the equimolar composition, we conducted a brief exploration of the quasi-ternary phase diagram of this composition. Contrary to the equimolar system we found here more frequently half-metals. By analyzing the projected density of states we were able to relate the metallic spin down channel to a dominant presence of manganese states around the Fermi energy. Inside the compositions that we tested, we found evidence for that there exists a positive relation between the band gap in this system, most notably in spin up, and compositions poor in chromium and/or rich in manganese. Specifically, we found two very positive compositions: $\text{Cr}_3\text{Fe}_3\text{Mn}_7\text{Ni}_3\text{Si}_{32}$ and $\text{Cr}_3\text{Fe}_5\text{Mn}_5\text{Ni}_3\text{Si}_{32}$, where the most stable supercell of the former displayed a spin up band gap of 0.47 eV, and the latter a total

band gap of 0.1 eV, with PBE.

Lastly, we tested various compositions where we introduced cobalt/titanium at the cost of either Cr, Mn or Ni. Based on the most stable configuration in each of these compositions, the only band gap we found in this experiment was a spin up band gap of 0.46 eV in $(\text{CrFeMnCo})\text{Si}_2$. By manually investigating the calculated eigenvalues of the different compositions, we were able to relate the metallic compounds to defect states in the band gap. This is a familiar term in random alloys, in which states at the band edges deviate slightly from completely full/empty occupancy. The effect and occurrence of defect states varied from composition to composition and supercell to supercell, for instance in the Cr:Fe:Mn:Ni:Si system, defects states was most prominent for spin down states, which resulted in several half-metallic structures.

In accordance with the spin polarization of the band gap, we noted a finite magnetic moment in most alloys. Distinctly, the equimolar alloy contained a magnetic moment of $0.083\mu_B$ in all five configurations of the equimolar alloy. Upon investigation of the local magnetic moments, we discovered that the magnetism was mainly attributed to chromium and manganese atoms in the lattice. This was found as a general trend for all alloys based on the FeSi_2 structure. Due to this severe spin polarization, a possible application of these alloys, particularly the Cr:Fe:Mn:Ni:Si alloys, could be could be as spintronics [16].

In terms of thermoelectric application, we find limited success in respect to the band gap. Recalling that good thermoelectrics are semiconductors with band gaps around 0.2 eV, we observe that the semiconducting band gaps of the $(\text{CrFeMnNi})\text{Si}_2$ are too small. However, we have found instances more suitable, such as the HSE06 band gap of 0.18 eV in one of the supercells. Furthermore, we can expect that the band gaps in the real material are larger than the PBE band gaps, thus there is a possibility that the $(\text{CrFeMnNi})\text{Si}_2$ alloy could be applied as a thermoelectric. Nevertheless, to qualitatively state the thermoelectric applicability of this compound, we would have to study properties such as the Seebeck coefficient, as well the thermal and electrical conductivity.

Chapter 10

Future work

In future studies of this system, I would first and foremost try to resolve several of the uncertainties circling the results presented in this project. This would include a more thoughtful investigation of the true ground state of the $(\text{CrFeMnNi})\text{Si}_2$ composition, by first testing multiple configurations and a larger number of SQS sizes to reduce variance and obtain a converged value of the band gap. Secondly, to decide on the most representative configuration we should have put more efforts into correctly/optimally specify the magnetic configuration of each SQS, and study excited states of the alloys to account for entropic contributions to the stability. Moreover, a test of different crystal structures in addition to the orthorombic CMCE space group of the $(\text{CrFeMnNi})\text{Si}_2$ alloy should be done, as the local minima method of DFT does not guarantee that this is the most stable conformation of the alloy.

The overarching motivation of this thesis have been to simply locate a band gap in high-entropy silicides, which by no means have been simple. However, now that we have located such a compound, in future work we would like to devote more effort into specifically analyze the band gap. Potentially try to plot and analyze the band structure of the alloy and qualitatively study the band gap by different functionals. Furthermore, we performed only a very limited search of the quasi-ternary phase diagram of the Cr:Fe:Mn:Ni:Si system, but found promising results in the direction of less chromium and more in manganese. Thus, a future study of more deliberate compositions in these directions would also be interesting. Provided that these results yielded positive outcomes of the band gap, suitable for thermoelectric application, future work could focus on a complete study of this material as a thermoelectric, and consider factors such as the Seebeck coefficient and electrical and thermal conductivity.

Appendix A

Figures

A.1 Density of states

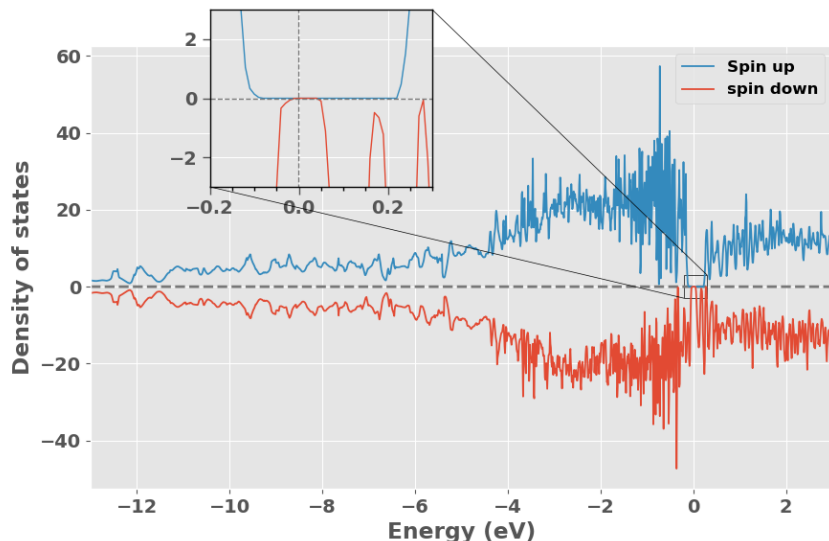


Figure A.1: Density of states SQS E (CrFeMnNi)Si₂ with PBE.

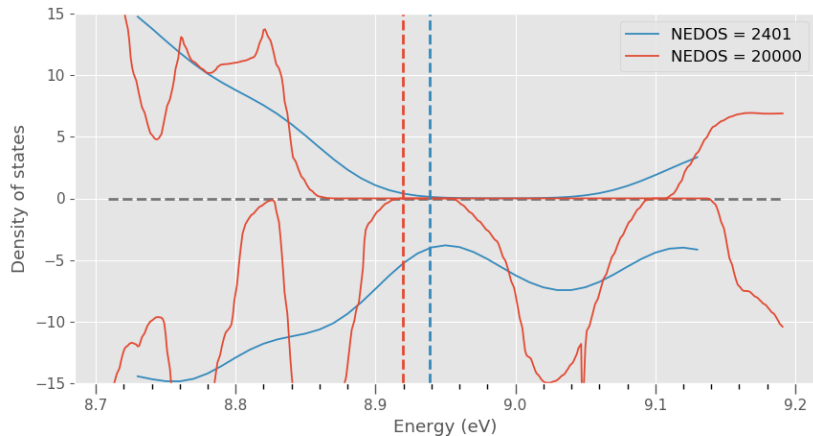


Figure A.2: Density of states SQS C ($\text{CrFeMnNi}\text{Si}_2$) with PBE. Nedos represent the number of points in the DOS calculation.

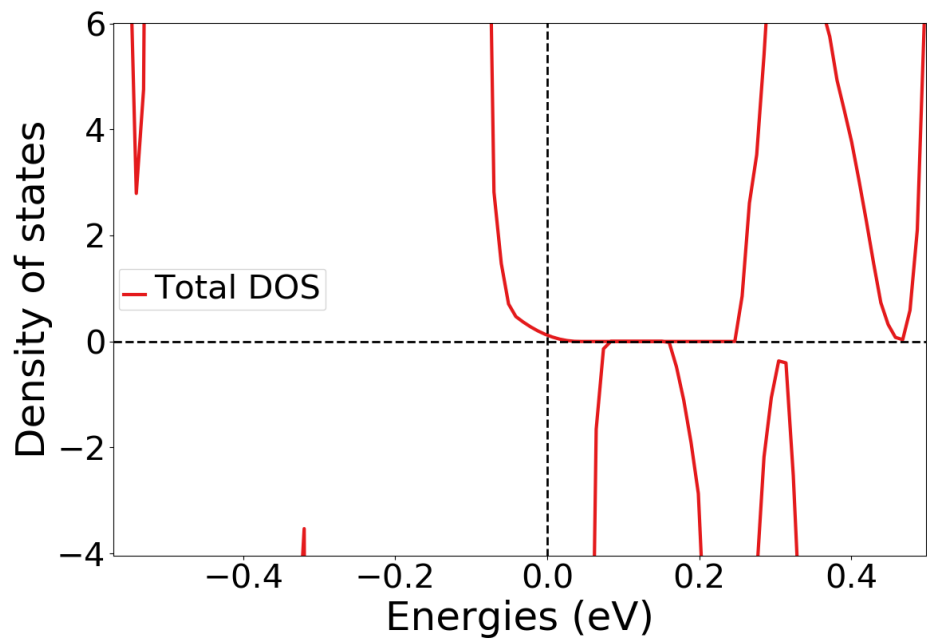


Figure A.3: Density of states SQS C $\text{Cr}_5\text{Fe}_5\text{Mn}_3\text{Ni}_3\text{Si}_{32}$, illustrating the small finite DOS at E_F due to the impurity gap.

A.2 Projected density of states

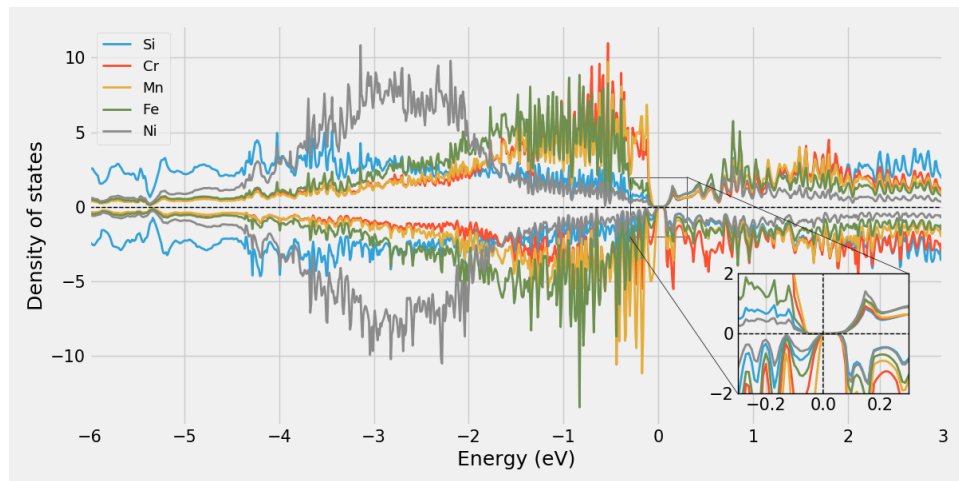


Figure A.4: Projected density of states SQS A

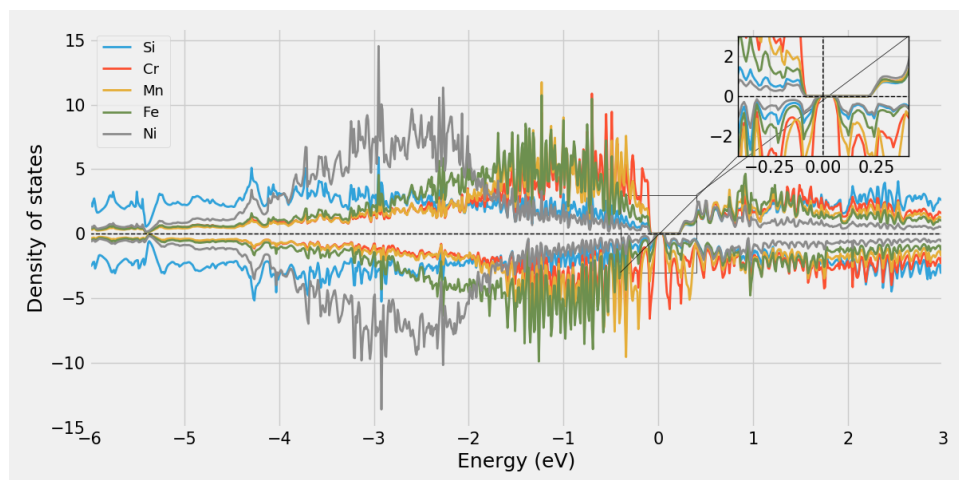


Figure A.5: Projected density of states SQS B

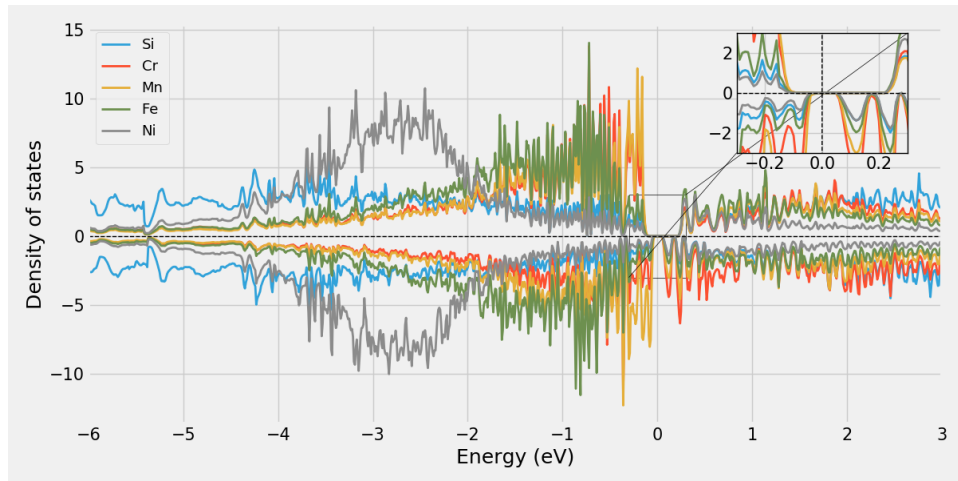


Figure A.6: Projected density of states SQS E

A.3 Charge density

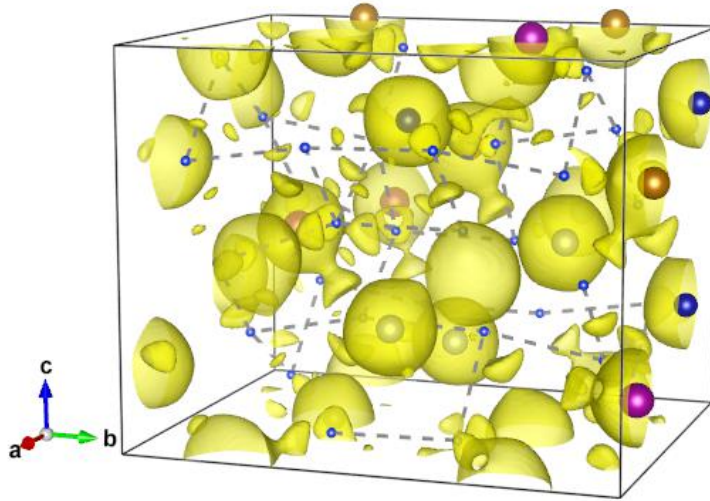


Figure A.7: Charge density of SQS C.

Bibliography

- [1] termoelektrisitet. *Velkommen til en termoelektrisk verden!* nor. Nov. 2013. URL: <https://termoelektrisitet.no/2013/11/24/velkommen-til-en-termoelektrisk-verden/> (visited on 24/11/2013).
- [2] Wikipedia. *Thermoelectric materials.* en. Page Version ID: 989933448. Nov. 2020. URL: https://en.wikipedia.org/w/index.php?title=Thermoelectric_materials&oldid=989933448 (visited on 22/11/2020).
- [3] Eddwi H. Hasdeo et al. ‘Optimal band gap for improved thermoelectric performance of two-dimensional Dirac materials’. In: *Journal of Applied Physics* 126.3 (July 2019), p. 035109. ISSN: 1089-7550. DOI: 10.1063/1.5100985. URL: <http://dx.doi.org/10.1063/1.5100985>.
- [4] G. Jeffrey Snyder and Eric S Toberer. ‘Complex thermoelectric materials’. eng. In: *Nature materials* 7.2 (2008), pp. 105–114. ISSN: 1476-1122.
- [5] Jorge Osvaldo Sofo and GD Mahan. ‘Optimum band gap of a thermoelectric material’. In: *Physical Review B* 49.7 (1994), p. 4565.
- [6] Tsai. Ming-Hung and Yeh. Jien-Wei. ‘High-Entropy Alloys: A Critical Review’. In: *Materials Research Letters* 2.3 (2014), pp. 107–123. DOI: 10.1080/21663831.2014.912690. eprint: <https://doi.org/10.1080/21663831.2014.912690>. URL: <https://doi.org/10.1080/21663831.2014.912690>.
- [7] Joshua Gild et al. ‘A high-entropy silicide: (Mo_{0.2}Nb_{0.2}Ta_{0.2}Ti_{0.2}W_{0.2})Si₂’. In: *Journal of Materiomics* 5.3 (2019), pp. 337–343. ISSN: 2352-8478. DOI: <https://doi.org/10.1016/j.jmat.2019.03.002>. URL: <https://www.sciencedirect.com/science/article/pii/S2352847819300334>.
- [8] Mari Mathillas Røsvik. *Structural Characterization of High Entropy Metal Silicide Alloys.* 2021.
- [9] Burkov. A. ‘Silicide Thermoelectrics: Materials for Energy Harvesting’. In: *physica status solidi (a)* 215 (June 2018). DOI: 10.1002/pssa.201800105.
- [10] S. J. Clark et al. ‘Structure and electronic properties of FeSi₂’. In: *Phys. Rev. B* 58 (16 Oct. 1998), pp. 10389–10393. DOI: 10.1103/PhysRevB.58.10389. URL: <https://link.aps.org/doi/10.1103/PhysRevB.58.10389>.

- [11] Voicu Popescu and Alex Zunger. ‘Effective Band Structure of Random Alloys’. In: *Phys. Rev. Lett.* 104 (23 June 2010), p. 236403. DOI: 10.1103/PhysRevLett.104.236403. URL: <https://link.aps.org/doi/10.1103/PhysRevLett.104.236403>.
- [12] R. Eppenga. ‘Ab initio band-structure calculation of the semiconductor β -FeSi₂’. In: *Journal of Applied Physics* 68.6 (1990), pp. 3027–3029. DOI: 10.1063/1.346415. eprint: <https://doi.org/10.1063/1.346415>. URL: <https://doi.org/10.1063/1.346415>.
- [13] H Lange. ‘Electronic properties of semiconducting silicides’. In: *physica status solidi (b)* 201.1 (1997), pp. 3–65.
- [14] ISMEAR - Vaspwiki. URL: <https://www.vasp.at/wiki/index.php/ISMEAR>.
- [15] Igor Levin. *NIST Inorganic Crystal Structure Database (ICSD)*. National Institute of Standards and Technology, 2018. URL: <https://doi.org/10.18434/M32147>.
- [16] Xingxing Li and Jinlong Yang. ‘First-principles design of spintronics materials’. In: *National Science Review* 3.3 (Apr. 2016), pp. 365–381. ISSN: 2095-5138. DOI: 10.1093/nsr/nww026. eprint: <https://academic.oup.com/nsr/article-pdf/3/3/365/31566317/nww026.pdf>. URL: <https://doi.org/10.1093/nsr/nww026>.